TITLE:

Mechanism and Structure-Guided Optimization of SLC1A1/EAAT3-Selective Inhibitors in Kidney Cancer

Authors: Pooneh Koochaki[1,*], Biao Qiu[2,3,*], Jesse A. Coker[4,5,*], Alexander Earsley[2], Nancy S. Wang[4], Todd Romigh[4], Christopher M. Goins[4,5], Carleigh Salem[1], Dehui Mi[6], Emily Days[6], Joshua A. Bauer[6], Shaun R. Stauffer[4,7,#], Olga Boudker[2,3,#], and Abhishek A. Chakraborty[1,7,8,#]

[1]Department of Cancer Sciences, Cleveland Clinic Research, Cleveland, OH 44195, USA

[2]Department of Physiology & Biophysics, Weill Cornell Medicine, New York, NY 10021, USA

[3]Howard Hughes Medical Institute, Weill Cornell Medicine, New York, NY 10021, USA

[4]Center for Therapeutics Discovery, Cleveland Clinic Research, Cleveland, OH 44195, USA

[5]Cleveland Clinic Lerner College of Medicine of Case Western Reserve University, Case Western Reserve University, Cleveland, OH 44106, USA

[6]Vanderbilt Institute of Chemical Biology, Vanderbilt University, Nashville, TN 37232, USA

[7]Department of Pharmacology, Case Western Reserve University, Cleveland, OH 44106, USA

[8]Case Comprehensive Cancer Center, Cleveland, OH 44106, USA

*equal contribution

[#]To whom correspondence should be addressed:

Shaun R. Stauffer (stauffs2@ccf.org)

Olga Boudker (olb2003@med.cornell.edu)

Abhishek A. Chakraborty (chakraa@ccf.org)

Abstract

Renal Cell Carcinomas (RCCs) depend metabolically on the trimeric sodium-coupled aspartate and glutamate transporter, SLC1A1/EAAT3; however, pharmacologically targeting SLC1A1 is challenging. We determined a cryo-EM structure of human SLC1A1 bound to compound **3e**, a recently described SLC1A1-selective bicyclic imidazo[1,2-α]pyridine-3-amine (BIA) inhibitor. **3e** binds a membrane-embedded allosteric pocket accessible only in the *apo* state, when SLC1A1 is unbound to substrate and sodium, and likely prevents sodium and substrate binding. Moreover, by wedging between the trimerization domain and the substrate-binding transport domain, alongside a cholesterol moiety from the lipid bilayer, **3e** blocks SLC1A1's elevator-like movements that are essential for transport. Mutations in this binding pocket abolish **3e** interaction and counteract **3e**'s cytotoxicity in RCC cells, confirming on-target activity and explaining SLC1A1 selectivity. A structure-guided medicinal chemistry effort yielded two new SLC1A1-selective BIA derivatives, PBJ1 and PBJ2, with enhanced cytotoxicity resulting from the inhibition of SLC1A1-dependent aspartate, glutamate, and cysteine metabolism.

Keywords: SLC1A1, EAAT3, cryo-EM, drug-resistant mutants, RCC, thermal shift assays, in silico docking, cellular IC_{50}, medicinal chemistry, impedance assays, FLIPR-based membrane potential analysis, metabolic regulation.

Introduction

Solute carriers (SLCs) are increasingly recognized for their roles in human diseases, including cancers (Hediger *et al*, 2013). Their localization to the cell surface makes them accessible to pharmacological agents, rendering them inherently druggable and therapeutically valuable. Furthermore, compared to normal tissues, the aberrant metabolic demands of tumors heighten their reliance on SLC activity, creating a therapeutic window for selective cancer targeting (Lin *et al*, 2015).

We previously identified SLC1A1 (also known as Excitatory Amino Acid Transporter 3, EAAT3) as an oncogenic dependency in clear cell Renal Cell Carcinomas (ccRCCs) (Grubb *et al*, 2025). ccRCCs are the most common form of adult kidney cancer and originate from the proximal tubule epithelial cells (Mitchell *et al*, 2018; Turajlic *et al*, 2018). Others have reported SLC1A1 as a metabolic vulnerability in fibrosarcoma (Yang *et al*, 2023), lung cancer (Guo *et al*, 2021; Wen *et al*, 2025), hematologic malignancies (Xiong *et al*, 2021), and brain tumors (Palos *et al*, 1996). SLC1A1 imports aspartate (L-Asp), glutamate (L-Glu), and, to a lesser extent, cysteine (L-Cys) from extracellular space (Bailey *et al*, 2011; Himi *et al*, 2003; Kanai & Hediger, 1992; Watts *et al*, 2014; Zerangue & Kavanaugh, 1996). L-Asp is essential for cancer cell growth because it provides the carbon skeleton for nucleotide biosynthesis (Sullivan *et al*, 2015). Moreover, L-Asp's poor cellular permeability and scarcity in hypoxic environments lead to increased dependence on its transporters in solid tumors (Birsoy *et al*, 2015; Garcia-Bermudez *et al*, 2018). L-Glu supports reductive carboxylation in hypoxic tumors and,

along with L-Cys, serves as a precursor for glutathione, aiding the oxidative stress response (Chen *et al*, 2024; Gameiro *et al*, 2013; Ling *et al*, 2023).

The SLC1A1 paralog, SLC1A2 (EAAT2), is predominantly expressed in the central nervous system (CNS), where it constitutes 1-2% of total protein in the forebrain (Danbolt *et al*, 2016; Danbolt *et al*, 1992). It is crucial for mammalian glutamate-mediated synaptic transmission and survival. In contrast, although SLC1A1 is broadly expressed and controls L-Asp/L-Glu reabsorption in the normal kidney, homozygous *Slc1a1* loss is well tolerated in mice. These mice show elevated urinary excretion of L-Asp and L-Glu (aminoaciduria); however, SLC1A1 loss does not cause neurodegeneration unless exposed to hypoxia or oxidative stress (Aoyama *et al*, 2008; Aoyama *et al*, 2006; Peghini *et al*, 1997). Similarly, SLC1A1 inactivation in humans results in aminoaciduria and minor cognitive symptoms, with minimal additional manifestations and a normal life expectancy (Bailey *et al.*, 2011). These observations suggest that global (and transient) SLC1A1 inhibition is likely safe in humans, supporting the development of selective inhibitors for cancer therapy.

All SLC1 transporters utilize an “elevator” mechanism for substrate uptake (**Fig. 1A**) (Canul-Tec *et al*, 2017; Canul-Tec *et al*, 2022; Kato *et al*, 2022; Qiu & Boudker, 2023, 2025; Qiu *et al*, 2021; Reyes *et al*, 2009). These homotrimeric carriers consist of a central trimerization or scaffold domain and a peripheral transport domain, which moves across the membrane from the outward-facing (OF) to the inward-facing (IF) position. In the OF conformation, the transport domains bind the substrate and co-transported Na^+

from the extracellular space, then translocate to the IF conformation to release them into the cytoplasm. During the return to the OF state, they translocate a K^+ ion from the cytoplasm to the outside, completing the cycle (Qiu & Boudker, 2023; Qiu *et al.*, 2021; Zerangue & Kavanaugh, 1996).

Most current SLC1 inhibitors are competitive L-Asp-derived compounds, such as DL-threo-β-benzyloxyaspartic acid (TBOA)(Shimamoto *et al*, 1998), and its trifluoromethyl-benzoyl derivative (TFB-TBOA)(Shimamoto *et al*, 2004), which lack selectivity and drug-like properties necessary for transition into the clinic. A recent study, however, described a series of bicyclic imidazopyridine amine (BIA) SLC1 inhibitors, with compound **3e** emerging as the best-in-class SLC1A1-selective agent (Wu *et al*, 2019). Notably, **3e** shares no structural similarity with SLC1A1's canonical substrates, raising questions about its on-target engagement and mechanism of action. Moreover, although **3e** inhibits cancer cell growth *in vitro*, it exhibits poor solubility and low kidney bioavailability (Grubb *et al.*, 2025). Lastly, **3e** contains an unsubstituted furan ring, making it vulnerable to hepatic clearance by the cytochrome P450 enzymes. Thus, **3e** is not suitable for *in vivo* use and limits opportunities for future clinical translation.

We report a cryogenic electron microscopy (cryo-EM) structure of human SLC1A1 bound to compound **3e**. Remarkably, **3e** occupies an allosteric pocket between the Na^+-binding site and the substrate-binding gate, accessible only in SLC1A1's *apo* state, unbound to Na^+ and substrate. The structure reveals the transporter in an IF *apo* state where **3e** and a cholesterol snuggle between the transport and scaffold domains. These

findings suggest a novel inhibition mechanism in which **3e** competes with Na^+ and substrate binding and likely traps the transporter in the IF conformation. Functional analysis reveals that F99 and T402 in SLC1A1 are key residues for **3e**-induced cytotoxicity, with the non-conserved F99 residue likely conferring selectivity towards SLC1A1. Structure-guided modifications of the BIA scaffold led to the identification of PBJ1 and PBJ2, two SLC1A1-selective inhibitors with improved cancer cell-killing potency. Genetic and metabolic rescue assays confirm that PBJ1 and PBJ2's cytotoxicity is on-target and stems from the depletion of key L-Asp-, L-Glu-, and L-Cys-derived metabolites. These findings reveal a previously unrecognized mechanism of SLC1 inhibition, providing a foundation for the development of SLC1A1-targeted therapies.

Results

Cryo-EM structure of SLC1A1/EAAT3 with Compound 3e

To assess **3e**'s mechanism of inhibition, we imaged recombinantly expressed human SLC1A1 with mutated glycosylation sites (SLC1A1g; see Methods) in the presence of 200 mM NaCl and 100 µM **3e** by cryo-EM. Particle alignment with imposed three-fold symmetry yielded an EM map at an overall resolution of 2.46 Å, revealing the transporter in an IF conformation (**Appendix Fig. S1 and Appendix Table S1**), similar to our previously reported structure (Qiu & Boudker, 2023; Qiu *et al.*, 2021). Since each protomer in the trimer functions independently (Grewer *et al*, 2005; Koch *et al*, 2007; Leary *et al*, 2007; Qiu *et al.*, 2021), we applied symmetry expansion and protomer classification without alignment, revealing three major structural classes (**Appendix Fig.**

S1 and Appendix Table S1). One class, resolved at 2.83 Å, pictured an IF protomer bound to Na^+ ions (**Fig. 1B**), indistinguishable from the previously reported Na^+-bound SLC1A1g structure (**Appendix Fig. S2A**). Two other classes (designated A and B), resolved at 2.56 and 2.76 Å, respectively, resembled the *apo* IF conformation of SLC1A1g determined in the absence of Na^+ ions and substrates (**Fig. 1C-E**). No density corresponding to **3e** was observed in the Na^+-bound protomers. In contrast, clear nonprotein density consistent with **3e** was present in both *apo* protomers (**Fig. 1D,E**), suggesting that **3e** either selectively binds to *apo* SLC1A1g or displaces bound Na^+.

To confirm the direct binding of **3e** to SLC1A1, we performed thermal shift binding assays using detergent-solubilized SLC1A1g. The protein was subjected to increasing temperature, and its unfolding was monitored using nano-differential scanning fluorimetry (nanoDSF). In a buffer containing 200 mM Na^+, SLC1A1g unfolded at ~69.1 ± 0.2°C. The addition of 100 µM **3e** produced a modest increase in the melting temperature of ~0.4 ± 0.3°C (**Fig. 1F; Appendix Fig. S2B**). In contrast, in Na^+-free, *apo* conditions, **3e** showed a more pronounced stabilization, with thermal shifts of ~1.8 ± 0.2°C (**Fig. 1F; Appendix Fig. S2C**), suggesting direct binding. These findings are consistent with our earlier cellular thermal shift assays (CETSA), in which we detected **3e**-induced SLC1A1 stabilization using extracts from human RCC cells expressing high levels of SLC1A1 (Grubb *et al.*, 2025). Together, with the structural data, these observations suggested that **3e** competes with Na^+ for binding to the carrier. Consistent with this, we found that **3e** led to a dose-dependent inhibition of Na^+ binding to the transporter, as measured by nanoDSF (**Fig. 1G**).

We further examined, using SLC1A1g heterologously expressed in HEK293 cells, whether inhibition by **3e** depends on extracellular Na^+ concentration. IC_{50} values were determined under saturating Na^+ concentrations (100 mM) or at a near-K_m concentration (20 mM). **3e** inhibited L-Asp uptake with IC_{50} values of 4.3 ± 0.5 µM at 100 mM Na^+ and 1.8 ± 0.7 µM at 20 mM Na^+, respectively (**Appendix Fig. S2D**), indicating relatively weak Na^+ dependence. Altogether, this behavior is consistent with tight binding of **3e** to the IF state and also likely reflects the relatively constant cytosolic Na^+ concentrations experienced by the transporter.

Compound 3e and cholesterol bridge transport and scaffold domains.

Closer inspection of the transport domain structure revealed that in both structural classes, A and B, **3e** binds within a pocket formed between transmembrane (TM) helix 3 (TM3) and the N-terminal helix of the helical hairpin 2 (HP2) (**Fig. 2A**). HP2 acts as a gate, controlling the access of substrates and ions to their binding sites (Alleva *et al*, 2020; Boudker *et al*, 2007; Focke *et al*, 2011; Riederer *et al*, 2022; Verdon *et al*, 2014). HP2 closes upon binding of the substrate, three co-transported Na^+ (Na1-3) ions and a proton, or counter-transported K^+ ions (**Fig. 1A**), facilitating the elevator-like movement of the transport domain. Whereas the **3e** binding pocket is open in *apo* and K^+-bound states, HP2 shifts closer to TM3 and obstructs the pocket in the Na^+-bound and L-Glu-bound states (**Fig. 2B-D**). TM3 harbors the conserved T101 and T102 residues, which, together with N366 and D368 in TM7, coordinate bound Na^+ in the Na3 site (**Fig. 2E**). When bound, **3e** forms a water-mediated hydrogen bond between its aniline NH and the

hydroxyl group of SLC1A1's T102 (**Fig. 2F,G**). Thus, **3e** and Na^+ in the Na3 site rely on the same T102 residue and favor different conformational states of the transporter.

In structural class A, we observed a well-resolved cholesterol molecule on the lipid-facing side of compound **3e** (**Fig. 2H**). Its headgroup was adjacent to the TM2-TM3 loop that links the scaffold and transport domains on the cytoplasmic side, while the hydrophobic sterol moiety was nestled between the drug and the scaffold domain. In the dominant class B, this site was occupied by glyco-diosgenin (GDN) – a detergent used during protein purification (**Fig. 2I**). Due to its larger size, GDN wedges more deeply into the crevice between the scaffold and transport domains, with its polar headgroup protruding beneath the TM2-TM3 loop. As a result, the transport domain swings slightly outward. In both structures, the hydrocarbon tails and parts of the sterol rings of cholesterol and GDN form intimate van der Waals contacts with **3e** on one side and the scaffold domain on the other. By contrast, no well-ordered lipid-like densities were observed at this site in the Na^+-bound IF SLC1A1g structure.

Because **3e** binds within the transport domain, it remained unclear whether it might also engage the *apo* OF state or K^+-bound conformations in which the **3e** binding pocket remains accessible (**Fig 2D**). To address this, we used the K269C/W441C SLC1A1g mutant, which can be trapped in a mixture of the OF state and an intermediate between the OF and IF states by Hg^{2+}-mediated cross-linking (Qiu & Boudker, 2023). Previously, we found that in the presence of KCl, the cross-linked mutant populates an *apo* OF state lacking bound K^+ ions and a K^+-bound intermediate state (Qiu & Boudker, 2023).

Cryo-EM analysis of this mutant in the presence of 300 mM KCl and 100 µM **3e** resolved two structural classes corresponding to these states, refined to ~3.1 Å and ~3.2 Å resolution and comprising ~80% and ~20% of particles, respectively. Neither class exhibited well-defined densities attributable to **3e** or cholesterol at the expected binding sites (**Appendix Fig. S3A,B**). Although a weak non-protein density was observed at the **3e**-binding site in the intermediate state, which was absent in the previous dataset without compound, it could not be convincingly assigned to **3e**. These observations suggest that, in the presence of K^+, **3e** either does not bind to this site with substantial occupancy and/or remains highly dynamic upon binding.

Our findings do not exclude the possibility that **3e** allows K^+ binding to the *apo* IF transporter, a step expected to occur rapidly following substrate and Na^+ release into the cytoplasm. We were unable to test this directly, as K^+ binding to the IF SLC1A1g is weak – at least under the detergent conditions used for cryo-EM – and the K^+-bound IF structure has not yet been resolved. Nonetheless, structural and functional data support a model in which **3e**, together with associated cholesterol, bridges the scaffold and transport domains, thereby impeding the elevator-like movements required for the transition from the IF state to the intermediate and OF conformations and effectively arresting the transport cycle. A conceptually related mechanism has been proposed for UCPH-101, an allosteric, non-competitive inhibitor selective for SLC1A3/EAAT1(Abrahamsen *et al*, 2013; Erichsen *et al*, 2010), which binds at the interface between the scaffold and transport domains in the OF state and prevents inward translocation of the transport domain (**Fig. 2J**) (Canul-Tec *et al.*, 2017).

Structural basis of 3e's SLC1A1 selectivity.

Most residues forming the **3e**-binding pocket are conserved across SLC1 paralogs, except for F99, which is unique to SLC1A1, and which interacts with ortho-methylaniline of **3e** (**Fig. 3A**). To probe the role of the F99 residue, we mutated it to leucine or methionine – residues found at the equivalent position in other SLC1 paralogs (**Fig. 3B**) – or to alanine as a control. Additionally, we mutated the conserved T402 residue, which forms a hydrogen bond with the core imidazopyridine ring of **3e**, to isoleucine or leucine. We evaluated these mutants using cell survival assays to assess **3e**-mediated inhibition of SLC1A1 and nanoDSF to assess direct binding to the transporter.

We first generated, using site-directed mutagenesis, a panel of the SLC1A1 mutants (**Table 1**) and then tested their functionality in a rescue assay. CRISPR/Cas9-mediated knockout of SLC1A1 (1A1sg5) causes antiproliferative effects in human kidney cancer cells, such as A498, but viability can be restored by introducing a sgRNA-resistant version of functional SLC1A1. Except for the F99A mutant, all F99 and T402 variants retained functionality and restored cell viability to levels comparable to WT SLC1A1 (**Fig. 3C**). We then used isogenic A498 cells expressing either WT or mutant SLC1A1, or GFP as a non-specific control, in the presence of endogenous SLC1A1 and cultured them with various doses of **3e**. All functional **3e**-binding site mutants resisted the cytotoxic effects of **3e**, whereas cells expressing WT SLC1A1, the non-functional F99A mutant, or GFP remained sensitive (**Fig. 3D**). Notably, survival of the latter two cell lines depends on the endogenously expressed SLC1A1, which is inhibited by **3e**.

We also introduced the F99L and F99M mutations into SLC1A1g. Both purified mutant proteins remained monodisperse in size exclusion chromatography (**Appendix Fig. S4A**) and exhibited thermal stability similar to WT in the nanoDSF assays, with *Ti* values of ~67.3 ± 0.5°C (F99M) and ~65.6 ± 1.8°C (F99L) (**Appendix Fig. S4B,C**). However, **3e** failed to stabilize these mutant proteins (**Fig. 3E**), consistent with substitutions at F99 disrupting **3e** binding. These results validate our cryo-EM structure and identify F99 as a key determinant of **3e**'s selectivity towards SLC1A1. Furthermore, these drug-resistant mutants confirm that **3e**'s cytotoxicity in kidney cancer cells is mediated through on-target inhibition of SLC1A1.

Structure-activity relationship (SAR) studies to identify new SLC1A1 blockers

Compound **3e** binds within a lipid-embedded hydrophobic pocket and, unsurprisingly, is itself highly hydrophobic with a cLogP of 5.4. The ortho-methylaniline moiety orients toward the selectivity-defining residue F99, while the 2-furanyl ring is positioned beneath the adjacent cholesterol molecule, engaging in an arene-H interaction with the sidechain of M367 and packing against I406 (**Fig. 2H, 3A**). This binding pose explains **3e**'s previously reported empirical SAR (Wu *et al.*, 2019). Decreasing **3e**'s overall lipophilicity by the addition of polar groups reduced its potency, likely due to compromised membrane penetration and inability to access the binding site. **3e** forms two hydrogen bonds with SLC1A1: one between the core N1 and the hydroxyl group of T402; and another – mediated by a well-resolved structural water – between the aniline NH and the hydroxyl of T102 (**Fig. 2F, 3A**). Consistent with this, removal of the N1

hydrogen bond acceptor substantially reduced **3e**'s inhibitory potency in the previous SAR (Wu *et al.*, 2019). The 8-bromo group of **3e** projects into a narrow hydrophobic shelf formed by I399 and A371 in HP2, and V106 in TM3. These key interactions explain why the removal of C8-substituents disrupted binding. Finally, only the C7-position of the imidazopyridine core is partially exposed to solvent, which likely explains why bulky substitutions at other positions, particularly at C5 and C6, result in reduced activity due to steric clashes with the protein wall.

Guided by these structural insights, we identified four key groups, R_1-R_4, in **3e** that were amenable to modifications (**Appendix Fig. S5A**) and designed a series of new BIA analogs. First, given potential concerns over the oxidative metabolism of the 2-furanyl group, we designed modifications that replaced this moiety (R_1). Second, we tested the possibility of replacing the aniline and phenyl substitutions at C3 (R_2). We maintained a hydrophobic moiety at the C8-position (R_3), preserving high cLogP, and retained the hydrogen bond with T402. We tested the possibility of introducing additional hydrophobic groups into the C7-position (R_4). Importantly, the buried C5- and C6-positions were left unsubstituted to avoid steric clashes. We computationally docked a virtual library of **3e** analog molecules into our cryo-EM structure and prioritized candidates with favorable poses and predicted free energies of binding lower than that of **3e**. Ultimately, we synthesized and evaluated ~40 BIA analogs (**Appendix Tables S2** and **S3**).

We screened the BIA compounds using two orthogonal approaches. First, we employed the nanoDSF assay to measure the ligand-induced thermal stabilization of SLC1A1g under Na^+-free conditions. As expected, **3e** stabilized the carrier by ~3.5ºC; however, vehicle control (DMSO), buffer control (N-methyl-D-glucamine, NMDG), and TFB-TBOA, whose binding depends on Na^+, had no measurable effect (**Fig. 4A**). The **3e** analogs exhibited a range of stabilizing effects, with 21 candidates increasing the melting temperature by at least 1°C (**Fig. 4A; Appendix Fig. S5B**). Second, we assessed the cytotoxicity of the compounds in the SLC1A1-dependent A498 cells using a high-throughput 384-well format assay over 7 days. Compared to the earlier 12-well, 14–20-day assay (**Fig. 3D**), the GI_{50} values were generally higher in the 384-well format, likely reflecting differences in assay duration and the metabolic state of the cells. Using **3e** as a reference, we identified ~20 analogs with greater potency (**Fig. 4B**). From these, we selected the most potent compounds (**12**, **10**, **30**, **38**, and **04**; **Fig. 4C,D**) that also stabilized SLC1A1g by more than 1°C in the nanoDSF assays for further validation. As a negative control, we also included the highly cytotoxic compound **14**, which did not bind to SLC1A1g in the thermal shift assays (**Fig. 4A**), suggesting it would display off-target (i.e., non-SLC1A1-mediated) cytotoxicity.

Identifying improved SLC1A1-selective BIA analogs

We first tested the selected analogs in two additional human RCC lines, UMRC-2 and 786O, which are less sensitive to SLC1A1 inhibition than A498 cells. Two compounds – **30** (featuring the C2-azetidine and C7-fluoro substitutions, hereafter referred to as PBJ1) and **38** (containing a C8-difluoromethyl substitution, hereafter referred to as

PBJ2) – demonstrated increased cytotoxicity in these cells compared to **3e** (**Fig. 5A-C**). When docked into the cryo-EM structure, both PBJ1 and PBJ2 occupied the **3e** binding pocket in poses virtually identical to **3e**, while extending into adjacent available cavities (**Fig. 5D**). Expressing drug-resistant SLC1A1 F99M and T402I mutants in A498 cells conferred resistance to PBJ1 and PBJ2 (**Fig. 5E**), mirroring their resistance to **3e** (**Fig. 3D**). In contrast, other tested analogs showed no improvements in potency in UMRC2 and 786O cells (**Appendix Fig. S6A,B**) and were cytotoxic for A498 cells expressing the drug-resistant mutants (**Appendix Fig. S6C**-**H**), suggesting that they might have off-target effects. Altogether, we discovered two new analogs – PBJ1 and PBJ2 – that were more potent on-target derivatives of **3e**.

The inactivation of the von Hippel-Lindau tumor suppressor protein (pVHL), which functions as a cellular E3 ligase, and the consequent chronic activation of pVHL's cellular substrate Hypoxia Inducible Factor α-subunit (HIFα), are molecular hallmarks of ccRCC (Ricketts *et al*, 2018). The HIF2α isoform, in particular, functions as a critical oncogenic driver in ccRCC (Gordan *et al*, 2008; Kondo *et al*, 2003), and pharmacological approaches to target this protein are now FDA approved for use in ccRCC patients (Chen *et al*, 2016; Cho *et al*, 2016; Jonasch *et al*, 2021; Wallace *et al*, 2016). Notably, SLC1A1 dependence in kidney cancer is HIF-independent (Grubb *et al.*, 2025), suggesting that targeting SLC1A1 might augment the cytotoxic effects of HIF2α blockade. To test this hypothesis, we treated the HIF2α-dependent A498 cell lines with combination doses of the HIF2α inhibitor (PT2385) and the SLC1A1 inhibitors (**3e**, PBJ1, and PBJ2). HIF2α inhibition causes cytotoxic effects only upon chronic treatment

for ~4-6 weeks *in vitro* (Cho *et al.*, 2016; Shirole *et al*, 2025). Consistent with this, we found relatively modest cytotoxic effects with PT2385 treatment alone (grey bars, **Fig. 5F-H**). However, we saw significantly higher toxicity upon combining PT2385 with the SLC1A1 inhibitors, especially the more potent PBJ1 and PBJ2, in both short-term assays with higher doses (**Appendix Fig. S6I**) and long-term assays with lower doses of the SLC1A1 inhibitors (**Fig. 5F-H**). Finally, in drug-drug interaction analysis using the SynergyFinder algorithm (Ianevski *et al*, 2022) we observed that these combination effects were synergistic, as evidenced by high Bliss synergy scores across various drug combinations (**Fig. 5I-K**).

Improved 3e Derivatives Block SLC1A1 Transport Activity

To directly assess the inhibition of SLC1A1's transporter activity, we performed two orthogonal assays. First, we measured cellular impedance using modified culture dishes with two electrodes that measure electron flow. L-Asp and L-Glu uptake causes cellular swelling to decrease current flow. This apparent increase in impedance due to cellular swelling can be used as a proxy for substrate uptake (**Fig. 6A**), as previously described (Sijben *et al*, 2022).

We generated monoclonal HEK293 cells with doxycycline (Dox) inducible expression of SLC1A1, SLC1A2, or SLC1A3 (**Fig. 6B**). HEK293-SLC1A1 cells demonstrated a time-dependent increase in impedance in the presence of L-Glu, reaching equilibrium at ~1 hour after substrate addition (**Fig. 6C; Appendix Fig. S7A,B**). Notably, these changes occurred only in the presence of Dox, which aligns with previous reports of low

endogenous expression of SLC1 transporters in the HEK293 cells (Sijben *et al.*, 2022), demonstrating their suitability for these impedance-based uptake assays. Compound **3e** inhibited the uptake of 1 mM L-Glu (**Fig. 6C; Appendix Fig. S7B**), 2 mM L-Glu (**Appendix Fig. S7C**), and 2 mM L-Asp (**Appendix Fig. S7D**), in a dose-dependent manner (**Appendix Fig. S7E**). In these assays, PBJ1 and PBJ2 showed IC_{50} values of ~10 μM, comparable to **3e**, while retaining >100-fold selectivity against SLC1A2 and SLC1A3 (**Fig. 6D; Appendix Fig. S7F**). By contrast, the TFB-TBOA competitive pan-SLC1 inhibitor (Shimamoto *et al.*, 2004), blocked uptake by all subtypes (**Fig. 6D; Appendix Fig. S7F**). Thus, PBJ1 and PBJ2 retain the SLC1A1 selectivity of the parent **3e** compound.

Next, we orthogonally validated our impedance assay by measuring changes in membrane potential triggered by SLC1A1-dependent L-Glu transport in the presence or absence of the SLC1A1 inhibitors. SLC1A1's ion coupled transport cycle involves the co-transport of Na^+ ions with L-Asp/L-Glu into the cell and an expulsion of K^+ ions (**Fig. 1A**). The ion transport cycle results in net changes in membrane potential, which can be measured using electrophysiology approaches or with specialized membrane potential dyes in Fluorescent Imaging Plate Reader (FLIPR) assays (Wu *et al.*, 2019). Using the Dox-inducible SLC1A1 system (**Fig. 6B**), we found that **3e**, PBJ1, and PBJ2 treatment diminished L-Glu-induced membrane potential changes in a dose-dependent manner, consistent with a blockade of the SLC1A1 transport cycle (**Fig. 6E,F**). As with the impedance assay, however, we did not notice any significant difference in IC_{50}s of the

three SLC1A1 inhibitors in this acute inhibitor assay, with all molecules showing half-maximal inhibition ~2-5 µM (**Appendix Fig. S7G**).

Metabolic contribution of the SLC1A1 inhibitors in kidney cancer cells

The three amino acids imported by SLC1A1 – L-Asp, L-Glu, and L-Cys – are precursors for critical metabolites in cancer cells. L-Asp provides the carbon skeleton for nucleotide biosynthesis; both L-Asp and L-Glu contribute towards the tricarboxylic acid (TCA) cycle; and L-Glu and L-Cys are precursors for glutathione (reduced: GSH; oxidized: GSSG) biosynthesis (**Fig. 7A**). To confirm the impact of the SLC1A1 inhibitors on L-Asp uptake, we first measured intracellular L-Asp uptake in the HEK293 cells with Dox-inducible SLC1A1. To this end, we cultured the cells in the presence of Dox and the SLC1A1 blockers and then measured intracellular L-Asp pools using a colorimetric assay (**Fig. 7B**). This assay converts L-Asp to pyruvate and then measures pyruvate abundance using a colorimetric probe. To control for basal intracellular L-Asp/pyruvate, we measured (and subtracted) the signal obtained from cells that were not exposed to Dox. Consistently, we observed that the SLC1A1 inhibitors reduced intracellular L-Asp pools, with PBJ1 and PBJ2 having more pronounced effects (**Fig. 7C**).

In the A498 cells treated the SLC1A1 inhibitors we observed reduced intracellular GSH and GSSG levels (**Fig. 7D,E**), consistent with diminished L-Glu and L-Cys uptake, and in line with our previous metabolomics data showing a prominent reduction in TCA cycle metabolites and GSH/GSSG following **3e** treatment in kidney cancer cells (Grubb *et al.*, 2025). Moreover, the reduction in GSH/GSSG levels correlated with the antiproliferative

effects of these compounds (**Fig. 7F**). Finally, supplementation with cell-permeable methyl ester derivatives of L-Asp (meAsp), L-Glu (meGlu), or GSH rescued the fitness defects caused by PBJ1 and PBJ2 (**Fig. 7G-I**). Altogether, these findings supported the conclusion that the antiproliferative activity of the BIAs emerged from metabolic perturbations directly linked to SLC1A1 inhibition.

Discussion

The SLC1 family includes five dicarboxylic amino acid transporters, EAATs, which differ in tissue distribution and physiological roles (Danbolt, 2001; Grewer *et al*, 2014; Kanai *et al*, 2013; Vandenberg & Ryan, 2013). All are expressed in the CNS, where SLC1A2/EAAT2 and SLC1A3/EAAT1 are primarily responsible for clearing synaptic L-Glu; their diminished activity leads to devastating neurological pathologies. SLC1A1/EAAT3's broader expression in peripheral tissues distinguishes it among EAATs. In the kidney proximal tubules, it mediates the reabsorption of L-Glu and L-Asp, becoming critical for sustaining the metabolic demands of kidney cancer cells. This metabolic reliance credentials SLC1A1 as a promising therapeutic target and underscores the need for SLC1A1-selective inhibitors.

Developing subtype-selective drugs for EAATs has been challenging because of the high conservation of their substrate-binding sites. Recent cryo-EM structures of SLC1A1-3 confirmed that these sites are nearly identical across paralogs, limiting the selectivity of orthosteric competitive inhibitors (Canul-Tec *et al.*, 2017; Canul-Tec *et al.*, 2022; Kato *et al.*, 2022; Qiu & Boudker, 2023, 2025; Qiu *et al.*, 2021; Zhang *et al*, 2022).

Moreover, such compounds are often ineffective under physiological conditions where substrate concentrations are high. In contrast, allosteric SLC1 inhibitors, such as the SLC1A3-selective UCPH-101 (Abrahamsen *et al.*, 2013; Erichsen *et al.*, 2010), hold greater therapeutic promise because they target less conserved sites and often act via non-competitive mechanisms, enabling subtype selectivity and sustained efficacy.

Growing recognition of SLC1A1's role in human disease has spurred efforts to develop selective inhibitors, leading to the discovery of the BIA series, including compound **3e** (Wu *et al.*, 2019). However, the structural basis for **3e**'s SLC1A1-selective inhibition remained unresolved. Our high-resolution cryo-EM structure revealed that **3e** binds to SLC1A1 in its IF *apo* state, outside of the substrate-binding site. It engages a membrane-embedded allosteric pocket and, together with a cholesterol molecule, wedges between the transport and scaffold domains. This binding mode resembles that of UCPH-101, which binds to the SLC1A3 transporter in its OF conformation at the domain interface and is thought to inhibit transport by blocking the elevator movements of the transport domain (Canul-Tec *et al.*, 2017). By analogy, **3e** may similarly block elevator movements, arresting the transporter in the IF state. However, unlike UCPH-101, **3e** also interferes with ion and substrate binding by engaging a residue that coordinates the Na^+ ion.

Prior structural studies have established that SLC1A1 functions as a highly dynamic molecular machine, undergoing complex conformational rearrangements throughout its transport cycle (**Fig. 1A**) (Qiu & Boudker, 2023, 2025; Qiu *et al.*, 2021). Importantly,

several proposed states, such as K^+-bound OF and IF conformations and K^+/Na^+-co-bound states (Kortzak *et al*, 2019; Wang *et al*, 2020; Wang *et al*, 2019), have not yet been structurally resolved. Our data nevertheless suggest that **3e** selectively targets a single state or a small subset of conformations, underscoring the importance of considering the full conformational landscape of SLC1 and other dynamic membrane transporters in the development of next-generation inhibitors.

Our structures further revealed that the F99 residue, which is not conserved in other SLC1 transporters, is a major determinant of subtype selectivity. Mutating F99 produced functional transporters that could not bind **3e**. These mutants, as well as mutants of T402, which is intimately involved in drug coordination, confer resistance to compound-induced cell death in RCC cell lines. These drug-resistant mutants are a gold-standard tool for demonstrating that **3e** and the newly identified PBJ1 and PBJ2 analogs act on-target in cellular assays. Consistently, metabolic rescue experiments revealed that PBJ1 and PBJ2 prevent cancer cell growth by directly blocking SLC1A1-dependent metabolic programs.

PBJ1 and PBJ2 compounds emerged from our structure-guided SAR campaign. Interestingly, while they showed improved on-target cytotoxicity compared to **3e** in cell assays, they did not exhibit increased affinity for SLC1A1 in nanoDSF or higher inhibitory potency in the impedance-based or FLIPR-based transport assays. This might be because the antiproliferative assays measure the impact of sustained SLC1A1 blockade over a period of 2-3 weeks. In contrast, the other assays measure more acute

effects occurring on time scales of minutes to hours. Moreover, unlike the other approaches, antiproliferative assays measure the cumulative impact of blocking the uptake of all SLC1A1 substrates. Altogether, the acute binding and inhibition assays can identify *bona fide* SLC1A1 inhibitors but might not perfectly capture the analog's cellular potency.

PBJ1 and PBJ2 have improved certain pharmacological features over the parental **3e** molecule. For instance, PBJ1 lacks the labile furan ring, whereas PBJ2 has the difluoromethyl replacement for bromine, which improves its 'drug-like' features. Given the membrane-embedded nature of the binding pocket, further optimization of these BIA inhibitors might prove challenging. Nevertheless, our findings provide the structural basis and the rigorous validation pipeline necessary for a more comprehensive search of new chemical scaffolds that target SLC1A1.

Methods

Protein expression and purification

The de-glycosylation (N178T, N195T) mutant of human SLC1A1/EAAT3 protein, termed SLC1A1g for short, and its K269C/W441C mutant were purified as previously described (Qiu & Boudker, 2023, 2025; Qiu *et al.*, 2021). In brief, 1L suspension FreeStyle™ 293-F cells at a density of 2.5 million cells per mL were transiently transfected with 3 mg DNA and 9 mg PEI 25K (*Polysciences*). After 18 hours, the cells were supplemented with 2.2mM of valproic acid. The cells were harvested after 48 hours post-transfection and resuspended in lysis buffer containing: 50 mM Tris-HCl (pH 8.0), 1 mM EDTA, 1

mM L-Asp, 1 mM Tris (2-carboxyethyl) phosphine (TCEP), 1 mM Phenylmethylsulfonyl fluoride (PMSF), and 1:200 dilution of protease inhibitor cocktail (catalog no. P8340, *Sigma-Aldrich*). The cells were disrupted using an EmulsiFlex-C3 homogenizer (*Avestin*) and the cell debris was removed by centrifugation at 10,000g for 15 min at 4°C. The membrane pellets were collected by ultracentrifugation at 186,000g for 1 hour at 4°C and solubilized in lysis buffer supplemented with 200 mM NaCl, 10% Glycerol, 1% Dodecyl-β-D-maltopyranoside (DDM, *Anatrace*), and 0.2% Cholesteryl hemisuccinate (CHS; *Sigma-Aldrich*) overnight at 4°C for SLC1A1g. The K269C/W441C mutant was solubilized in 2% DDM with 0.4% CHS for 1 hr at 4 °C. The insoluble material was removed by ultracentrifugation 186,000g for 1 hour at 4°C; the supernatant was then incubated with Strep-Tactin Sepharose resin (*GE Healthcare*) for 1 hour at 4 °C. The resin was washed with 8 column volumes of buffer containing 50 mM Tris-HCl (pH 8.0), 200 mM NaCl, 1 mM L-Asp, 1 mM TCEP, 5% glycerol, and 0.06% glyco-diosgenin (GDN, *Anatrace*), and the protein was eluted with 4 column volumes of the same buffer supplemented with 2.5-5 mM D-desthiobiotin (*Sigma-Aldrich*). The N-terminal Strep II and GFP tags were cleaved by incubating the protein with Prescission protease overnight at 4°C at a 40:1 w:w ratio. The SLC1A1g protein was further purified in "*apo*" condition by size-exclusion chromatography (SEC) in a buffer containing: 20 mM HEPES-Tris (pH 7.4), 100 mM N-methyl-D-glucamine (NMDG) chloride, 1 mM TCEP, and 0.01% GDN. The K269C/W441C mutant was purified by SEC in a buffer containing: 20 mM HEPES-Tris (pH 7.4), 200 mM NaCl, 1 mM L-Asp, and 0.01% GDN. The fractions containing the protein were combined, concentrated to ~0.5 mg/mL, and incubated with a 20-molar excess of $HgCl_2$ for 30 minutes at room temperature.

Following incubation, the crosslinked sample (SLC1A1g-X, for short) was purified by SEC in a buffer containing: 20 mM HEPES-Tris (pH 7.4), 300 mM KCl, and 0.01% GDN.

Thermostability assays

Purified *apo* SLC1A1g was concentrated to ~100 µM and then diluted 20-fold in a buffer containing 50 mM Hepes-Tris pH 7.4, 100 mM NMDG-Cl, and 0.01% GDN, without or with supplementation with 100 µM **3e** or other drugs dissolved in DMSO. During the screening of **3e** analogs, the final mixtures contained 10% DMSO, whereas in the initial **3e** binding experiments, the DMSO concentration was 1%. NMDG-Cl was 200 mM in these experiments. The thermostability assay was performed using Tycho NT.6 (*NanoTemper Technologies*). In brief, protein samples were heated from 35°C to 95°C at 30°C/min, and the intrinsic fluorescence of the protein was recorded at 330 nm and 350 nm. The ratio of fluorescent signals at 350 and 330 nm, its first derivative, and the inflection temperature (*Ti*) were calculated by the Tycho NT.6 software. All measurements were repeated on at least two indepdent protein preps and three technical replicates.

Cryo-EM sample preparation and data acquisition

Purified *apo* SLC1A1g was supplemented with 200 mM NaCl and 100 µM compound **3e,** and SLC1A1g-X was supplemented with 100 µM **3e** only. Samples were concentrated to about 4 mg/mL at room temperature. 3.5 µl sample was applied to glow-discharged QUANTIFOIL R1.2/1.3 holey carbon-coated 300 mesh gold grids (*Quantifoil*, *Großlöbichau*). The grids were blotted for 3 seconds at room temperature

and 100% humidity and plunge-frozen into liquid ethane using a Mark IV Vitrobot (*FEI*). The cryo-EM dataset for SLC1A1g with **3e** was auto-collected using Leginon (Suloway *et al*, 2005) on Titan Krios equipped with a 20 eV energy filter and Gatan K3 camera at the Columbia University Cryo-Electron Microscopy Center. A total of 9,970 movies were collected at a nominal magnification of 100,500-fold with a calibrated pixel size of 0.83 Å in counting mode. A nominal defocus value of -1.0 to -2.0 µm and a total dose of 58 $e^-/Å^2$ over 50 frames were applied during data collection. The data on SLC1A1g-X in KCl with **3e** were collected similarly using Titan Krios equipped with a 20 eV energy filter and Gatan K3 camera at the New York Structural Biology Center. A total of 9,146 movies were collected at a nominal magnification of 81,000-fold with a calibrated pixel size of 0.43 Å in super-resolution mode. A nominal defocus value of -0.8 – -2.5 µm and a total dose of 53.9 $e^-/Å^2$ over 55 frames were applied to the data collection.

Cryo-EM image processing

The cryo-EM dataset for SLC1A1g with NaCl **3e** was processed using a combination of Relion 3.1.0(Scheres, 2012) and CryoSPARC v4.2.1(Punjani *et al*, 2017). The movies were aligned using Motioncor2 in Relion, and the micrographs were imported into CryoSparc. The CTF parameters of the micrographs were estimated using Path CTF, and micrographs with the CTF fit resolution worse than 6 Å were removed from the dataset. About 6.7 million particles were picked from 9,594 images, and ~2.7 million particles were extracted using a box size of 160 pixels with 2x binning after particle inspection. The particles were subjected to 2D classification, and 945 K particles exhibiting secondary structure features were selected and subjected to two rounds of *ab*

initio reconstructions. 303 K particles producing a volume with the most features were further refined to 3.4 Å by nonuniform refinement (hereafter, NUR) with C1 symmetry. Separately, 162 K particles extracted from 500 micrographs were subjected to 1–10 iterations of *ab initio* reconstructions to generate 5 decoy volumes. After removing nonprotein junk particles in the 2D selection step, about 2.5 million particles were subjected to heterogeneous refinement using one good volume (3.4 Å from the last step NUR) and 5 decoy volumes for cleaning (heterogeneous refinement cleaning, HRC). After that, 589 K selected particles were re-extracted with a box size of 320 pixels without binning and subjected to HRC with C1 and NUR with C3 symmetry. Then, the particles were imported into Relion using PyEM (doi.org/10.5281/zenodo.3576630) for polishing. The polished particles were reimported into CryoSparc and subjected to HRC and NUR. After 2 rounds of polishing, HRC, and NUR steps, 556K particles were refined to 2.46 Å using C3 symmetry. Symmetry expansion and local classification were performed in CryoSPARC, with a mask applied over the protomer to resolve conformational heterogeneity. Three protomer conformations were further locally refined to 2.56 Å (*apo* IF with bound **3e** and GDN), 2.76 Å (*apo* IF with bound **3e** and cholesterol), and 2.83 Å (Na^+-bound IF) in CryoSPARC. The cryo-EM dataset for SLC1A1g-X with KCl and **3e** was processed using CryoSPARC v4.4.1. Briefly, the movies were imported into CryoSPARC and aligned using Patch Motion Correction with 2x binning. CTF parameters were estimated using Path CTF, and micrographs with the CTF fit resolution worse than 5 Å were discarded. About 2.2 million particles were extracted from 8,795 images using a box size of 150 pixels with 2x binning and were subjected to 2D classification. 912K particles exhibiting secondary structure features

were selected and subjected to one round of *ab initio* reconstructions. From these, 618K particles producing a volume with the most features were further refined to 3.64 Å by NUR with C1 symmetry (good volume). Separately, 98K particles showing non-protein features were subjected to 1–10 iterations of *ab initio* reconstructions to generate 5 decoy volumes. Then, the 912K particles were subjected to two rounds of HRC using one good volume and 5 decoy volumes. After that, 387K selected particles were refined by NUR and re-extracted with a box size of 300 pixels without binning. The unbinned particles were subjected to HRC with C1 and NUR with C3 symmetry; the resulting 329K particles were subjected to Reference-Based Motion Correction for polishing and finally refined to 3.11 Å by NUR with C3 symmetry. Then, symmetry expansion and local classification were performed in CryoSPARC, with a mask applied over the protomer to resolve conformational heterogeneity. Two protomer conformations were further locally refined to 3.11 Å (~80% particles, iOFS bound to K^+) and 3.23 Å (~20% particles, *apo* OFS) in CryoSPARC.

Model building and refinement

The IF *apo* and Na^+-bound SLC1A1g structures (PDB codes: 6X3F and 6X2L, respectively) were fitted into EM density maps using ChimeraX (Goddard *et al*, 2018). The models were manually adjusted in COOT (Emsley *et al*, 2010) and subjected to real-space refinement in Phenix (Adams *et al*, 2010). Structural model validation was performed in Phenix, and structural figures were prepared using ChimeraX. The Cryo-EM maps and atomic coordinates have been deposited in the Electron Microscopy Data Bank (EMDB) and Protein Data Bank (PDB) under accession codes: SLC1A1g class A

(*apo* IF with bound **3e** and cholesterol, EMD-71288, PDB-9P4X), class B (*apo* IF with bound **3e** and GDN, EMD-71289, PDB-9P4Y), and class C, (Na^+-bound IF, EMD-71290, PDB-9P4Z), SLC1A1g-X in iOFS with bound K+ ion (EMD-75048) and apo OFS (EMD-75049).

Radiolabeled L-Asp uptake

100mL of FreeStyle™ 293-F cells were transfected at a cell density of $1x10^6$ cells/mL with a plasmid encoding SLC1A1g as described above for large-scale protein production. 48 hours after transfection, cells were harvested by centrifuging at 200 g for 15 minutes at 4 °C and washed twice with 2 mL of resting buffer containing 11 mM HEPES-Tris (pH 7.4), 140 mM Choline chloride, 4.7 mM KCl, 2.5 mM $CaCl_2$, 1.2 mM $MgCl_2$, and 10 mM D-glucose. 200 µL of cells were then diluted fivefold to a final concentration of 1.0E07 cells/mL in resting buffer and prewarmed in a water bath to 37°C for at least 10 minutes. To start the reaction, 40 µL of resuspended cells were diluted fivefold in the same buffer, with 140 mM choline chloride replaced by either 20 mM NaCl and 120 mM Choline chloride or 100 mM NaCl and 40 mM Choline chloride, supplemented with appropriate concentrations of **3e**. After a 10-minute pre-incubation, uptake reactions were initiated by adding 0.5 µM L-[^{3}H]-Asp (*American Radiolabeled Chemicals, Inc.*) and 19.5 µM L-Asp. The reactions were incubated at 37°C for 45 seconds and terminated by mixing with 2 mL of ice-cold quench buffer containing 140 mM Choline chloride and 11 mM HEPES-Tris (pH 7.4). These mixtures were filtered over 0.8 µm nitrocellulose filters (*MF-Millipore*) and washed with 6 mL of ice-cold quench buffer. The filter was then placed into scintillation fluid, and the retained

radioactivity was quantified using a scintillation counter (*Beckman Coulter LS6500*). The uptake assays were performed on two independently prepared samples, each with two technical repeats.

Cell lines

A-498 (RRID: CVCL_1056), HEK293 (RRID: CVCL_0045), HEK293T (RRID: CVCL_0063), and 786-O (RRID: CVCL_1051) cells were obtained from the American Type Culture Collection. UMRC-2 (RRID: CVCL_2739) cells were obtained from Dr. Bert Zbar and Dr. Marston Linehan (National Cancer Institute). All cells were maintained in Dulbecco's Modified Eagle's Medium (DMEM) (Life Technologies 11995073) supplemented with 10% Fetal Bovine Serum (FBS) (Life Technologies 10437-028), and 1X Penicillin-Streptomycin (Life Technologies 15140163). Cells stably expressing cDNAs or sgRNA were generated by lentiviral infection followed by selection with Puromycin (2 µg/mL) or Blasticidin (10 µg/mL), as appropriate. HEK293$^{SLC1A1/SLC1A2/SLC1A3}$ cell lines were cultured in high-glucose Dulbecco's Modified Eagle Medium (DMEM, CCF Media Core) supplemented with 10% heat-inactivated Fetal Bovine Serum (FBS) (Gibco A5256801), 5 U/mL Penicillin/Streptomycin (Sigma P3032 & Gibco 11860), 2 mM L-glutamine (CCF Media Core), and 0.8 mg/mL puromycin (Phytopure^{TM}, MP Biomedicals 0219453925). All cells were grown at 37°C in 5% CO_2. Cell lines were periodically tested for mycoplasma and cell line identity was confirmed using STR analysis by the Cleveland Clinic's Cell and Media Core facility.

Lentiviral Infections

Lentiviral particles to introduce cDNAs or sgRNAs into cells were produced from HEK293T packaging cells. In a standard experiment, we seeded ~1.6E06 - 2.0E06 HEK293T cells into a 6 cm dish and transfected these cells with a transfection mix that contained 3 µg total DNA [1.5 µg lentiviral plasmid + 1.5 µg helper plasmids – psPAX2 (RRID: Addgene_12260) and pMD2.G (RRID: Addgene_12259) mixed in a 3:1 ratio] and 9 µl lipofectamine 2000 (Invitrogen 11668019). The transfection mixtures were prepared and incubated at RT for 20 minutes and then added dropwise onto cells. Cells were incubated for sixteen hours, following which the media was changed. Viral supernatant was collected at 48- and 72-hours post-transfection, combined, and filtered (0.45 µm). Aliquots were stored frozen at -80°C. To transduce recipient cells, we seeded 6-well plates with 1.5E05 – 2.0E05 cells and transduced them with 0.5 mL of the lentiviral supernatant in the presence of 8 µg/mL polybrene. The plates were returned to the incubator for 16 hours, after which the media was replaced, and cells were grown for an additional 24 hours prior to selection with the appropriate antibiotic.

Generation of SLC1A1 Mutant Constructs

Entry vectors and pLX304 constructs encoding sg5-resistant versions of SLC1A1 were previously described (Grubb *et al.*, 2025). Mutations encoding F99A, F99M, F99L, T402I, and T402L were generated in the sg5-resistant backbone either using overlap-extension PCR or by site-directed mutagenesis (Quickchange II XL; Agilent 200521) using the oligos described in the primer list. All mutant clones were verified by Sanger sequencing. Engineered clones were lentivirally transduced into recipient cells using the procedures described above. For the genetic rescue experiments to assay SLC1A1

functionality, cells were first engineered to express the sgRNA-resistant versions of either WT or mutant SLC1A1 (or GFP, as a control) in the pLX304 backbone (RRID: Addgene_25890). Following selection with blasticidin (10 µg/mL, 7-10 days), cells were lentivirally transduced with CRISPR/Cas9 constructs targeting SLC1A1 (1A1sg5) or a non-targeting control and selected with puromycin (2 µg/mL, 3 days). The sgRNA sequences are provided in the primer list. Following the second selection, equal number of viable cells were seeded at low density (typically, 100-200 cells/well of a 12-well plate) and cultured for 1-2 weeks post selection before staining the wells with crystal violet (0.25% in 20% methanol, stained overnight at 4˚C).

High Throughput Screening Assay for Compound 3e and Its Analogs

A two-fold serial dilution of each test compound was prepared in 100 % DMSO starting at 25 mM. White tissue culture 384-well plates were first pre-filled with 30 µL of complete DMEM with 1 mM L-Glu. Next, 100 nL of each compound dilution was acoustically dispensed into the plates in triplicate with a Labcyte Echo 550; vehicle (0.2 % DMSO final) and compound **3e** served as negative and positive controls, respectively. Finally, A 498 were seeded by adding 20 µL of a 2.5 × 10 cells /mL suspension (≈ 500 cells per well) using an E1 ClipTip electronic multichannel pipette, bringing the total well volume to 50 µL while maintaining 0.2 % DMSO. Plates were incubated for seven days at 37°C, 5 % CO2. Cell viability was measured by adding 25 µL CellTiter Glo® 2.0 reagent (Promega G7571) to each well, shaking for five minutes at 600 rpm, incubating ten minutes at room temperature, and recording luminescence on a Revvity EnVision multimode plate reader. Luminescence in the

vehicle-treated wells was normalized to 100% and used to perform regression analysis and establish each inhibitor's GI50, using the built-in algorithms in Graphpad prism (e.g., log-inhibitor versus response – variable slope).

Cytotoxicity assays using SLC1A1 Inhibitors

Cytotoxicity assays were used to evaluate the potency and on-target effects of the new SLC1A1 inhibitors (Cmpd **3e** analogs). To compare potency in human clear cell Renal Cell Carcinoma (ccRCC) cell lines, such as A 498, UMRC2, and 786 O, cells were seeded into 96 well plates (200 cells/well in 100 µL DMEM) and allowed to attach overnight. Serial two-fold dilutions of each test inhibitor were prepared in 100 % DMSO and diluted into complete medium to yield final inhibitor concentrations between 0.8 to 50 µM, each in 0.1 % (v/v) DMSO. Overnight culture media was aspirated and 200 µL of the appropriate drug containing media was gently added to each well.

To test on-target effects of each inhibitor, A-498 cells expressing either wild-type, F99M, or T402I SLC1A1 mutants (or GFP expressing controls) were seeded (100 cells/well in 1 mL volume) in a 12 well tissue culture plate. After 16 h to allow attachment, cells were exposed either to test compounds (final concentrations as indicated) or to 0.1 % (v/v) DMSO vehicle (negative control). The medium—including fresh compound or DMSO—was replaced every three days to ensure continuous treatment. After 21 days, colonies were trypsinised and viable cell numbers were counted using a Vi-Cell to assess the effects of treatment. Three independent biological replicates were statistically compared.

For metabolic rescue experiments, 3.0E05 A-498 cells were cultured in the presence of esterified L-Asp (meAsp, 100 µM), esterified L-Glu (meGlu, 100 µM), reduced Glutathione (GSH, 1 mM), or untreated (controls) for 3 days. The cells were then trypsinized, counted, and reseeded (1000 cells /well in a 12 well plate). The cells were cultured in the presence of the indicated supplements (or untreated controls) and PBJ1 or PBJ2 (0, 1.5, 3.0, or 6.0 µM for 2-3 weeks with media changes every 3-4 days. Fresh inhibitor and metabolite supplements were added at each media change. Cell counts were measured using the Vi-Cell counter and three independent biological replicates were statistically compared to evaluate differences.

Generation of HEK293$^{SLC1A1/SLC1A2/SLC1A3}$ Monoclonal Cell Lines

Full-length, human, mammalian codon-optimized SLC1A1 (#161044), SLC1A2 (#161067), and SLC1A3 (#161055) entry clones were obtained from AddGene. The SLC1Ax coding sequences were PCR amplified with compatible overhangs and cloned by a HiFi assembly (NEB) into a custom pPB-TetOn-Puro-SLC1Ax/3xGS/3xFLAG_SLC1Ax/P2A/EGFP (Vector Builder). This construct allows stable integration, via the PiggyBac® system, of a Dox-inducible SLC1Ax-3xFLAG cassette alongside a post-translationally released (P2A) EGFP. All three constructs were confirmed by whole-plasmid sequencing (Plasmidsaurus).

Parental HEK293 cells were co-transfected with pPB-TetOn-Puro-SLC1Ax/3xGS/3xFLAG_SLC1Ax/P2A/EGFP plasmids and SPB-DNA (Hera Biolabs) at

a 3:1 ratio with Fugene HD (Promega) per manufacturer's instructions. After 24 hours, the transfection media was replaced with full cell culture media supplemented with 0.8 mg/mL puromycin, and stably transfected pools were established after 5 days of selection.

For the establishment of monoclonal lines, each SLC1Ax selected pool was first enriched for high doxycycline-induced GFP expression by flow sorting using a ThermoFisher Bigfoot Spectral Cell Sorter. Each pool was seeded in full cell culture media in 2 T-175 flasks. At 80% confluence, cells were treated with 0.15 mg/mL doxycycline or vehicle for 24 hours. $3x10^7$ cells were harvested from each flask and resuspended to $1x10^7$ cells/mL in cell sorting buffer: 1X Phosphate buffered saline (Ca^{+2}/Mg^{+2} free), 1 mM EDTA, 25 mM HEPES pH 7.0, 1% FBS. A separate T-75 flask of parental HEK293 cells was also harvested and resuspended in cell sorting buffer to facilitate the definition of the (+) GFP gate. The top 4-6% GFP-expressing cells within the (+) GFP gate were sorted and plated at 1 cell/well in full cell culture media supplemented with 0.8 mg/mL puromycin in 96-well plates. 10-15 clones each for SLC1A1, SLC1A2, and SLC1A3 were expanded to T-75 flasks and tested for responsiveness in cell impedance measurements upon addition of 1 mM L-glutamate. SLC1A1 Monoclonal #6, SLC1A2 Monoclonal #5, and SLC1A3 Monoclonal #1 were used in reported impedance assays.

Impedance Assay

785 The impedance assay was conducted as previously described (Sijben *et al.*, 2022).
786 Briefly, HEK293^{SLC1A1}, HEK293^{SLC1A2}, and HEK293^{SLC1A3} monoclonal lines were
787 passaged in complete DMEM media (2 mM L-glutamine). On Day 1 of the assay, a
788 modified assay media containing DMEM with only 1 mM (0.5X) L-glutamine was
789 prepared, and 50 µL was added to each well of an E-Plate 96 PET plate (Agilent,
790 300600910) and incubated at RT for at least 30 minutes. HEK293^{SLC1Ax} cells were split
791 as standard into assay media and further diluted to a final concentration of 1.2E06
792 cells/mL. Once the cells were prepared, the E-Plate containing only media was placed
793 in an xCELLigence RTCA (Agilent), and a background reading was taken. The plate
794 was removed from the block, and 50 µL of cell suspension was added to each well, at a
795 final concentration of 6.0E04 cells/well in 100 µL of assay media. Cells were incubated
796 at room temperature for 30 minutes and then placed back onto the xCELLigence
797 overnight. Readings were taken every 5 minutes until the completion of the assay.
798
799 On the morning of Day 2, a 450 ng/mL solution of doxycycline was prepared by adding
800 0.675 µL of a 10 mg/mL DMSO stock of doxycycline to 15 mL of DMEM complete media
801 containing 10% FBS, 50 I.U. pen/strep, but without L-glutamine. 50 µL of doxycycline
802 was added per well to achieve a final concentration of 150 ng/mL, and SLC1Ax
803 induction was allowed to proceed for 6-8 hours. Compound serial dilutions (1:2 in 100%
804 DMSO) were prepared at a 1,000X top dose. 0.8 µL of the serially diluted compounds
805 were added to 200 µL of L-glutamine-free assay media and mixed well. 50 µL of the
806 compounds diluted in media (now 4X) were then added to the plate in technical

duplicates. To columns 1 and 12, media containing the equivalent amount of DMSO was added, and the plate was returned to the xCELLigence overnight.

After 16 to 20 hours (Day 3), 10 µL of a 21mM (21X) PBS stock of L-glutamate (Sigma Aldrich 49621) was prepared fresh and added to a final concentration of 1 mM to columns 2 through 12. 10 µL of PBS only was added to column 1 as a vehicle control. For the comparison of L-Glu vs. L-Asp, a 42 mM stock was prepared, and the final concentration of agonist was 2 mM. The E-Plate was returned to the xCELLigence, and readings were continued for three hours post-stimulation.

For data analysis, raw cell index (CI) values were normalized to time = 0 (the last reading before L-Glu addition) within each well, and then the background vehicle response in PBS-stimulated cells (column 1) was subtracted to generate nCI values. The AUC from the nCI time-course (over 3 hours) was extracted and plotted against log[compound] to extract IC_{50} values by non-linear regression using GraphPad Prism (v10). The maximum response in L-Glu stimulated cells (column 12) was set as the top of the curve.

Panoptic FLIPR Membrane Potential Assay

The HEK293-SLC1A1 cells were cultured in growth media containing DMEM (Gibco #11960-044), 10% heat-Inactivated FBS (Gibco #A5256801), 50 unit/mL Pen and 50 µg/mL Strep (Gibco #15140-122), 1 mM Sodium Pyruvate (Gibco #11360-070), and 1

mM L-Glutamine (Gibco #25030081). Additionally, 0.83 µg/mL of Puromycin (MP Biomedicals #0219453925) was added freshly to the growth media.

Cells were seeded into amine coated 384 well plates (Corning PureCoat #356719) at 15,000 cells/20 µL/well, with the plating media. The plating media contains the same components as the growth media except that 10% heat-Inactivated FBS was replaced by 10% Dialyzed FBS (Gibco #26400-044). Where relevant, Doxycycline (Alfa Aesar #J63805.06) was added to the cells at a final concentration of 0.15 µg/mL, following which cells were incubated at 37 °C, 5% CO_2 overnight.

Test compounds, L-Glu, and the membrane potential dye powder (Molecular Devices FLIPR Membrane Potential Assay Kit, RED, Explorer format # R8126) were prepared in KREBS buffer [140 mM NaCl (Sigma #S-9888), 4.7 mM KCl (Sigma #P3911), 2.5 mM $CaCl_2$ (Sigma #C3306), 1.2 mM of $MgCl_2$ (Sigma #M8266), 11 mM of HEPES (Gibco #15630-060), and 10 mM D-glucose (Sigma #G7528)].

The SLC1A1 inhibitors (10 mM in DMSO) were loaded into an Echo Qualified Low Dead Volume source plate (Labcyte #LP-0200) using an acoustic liquid handler Echo 650 (Beckman Coulter Life Sciences, Indianapolis IN 46268) in a 10-point dose range (38 nM to 75 µM) in quadruplet. The membrane potential dye was diluted by 2-fold using Krebs buffer, resulting in a (0.5x) dye concentration and 40 µL/well of this compound dilution buffer was dispensed into the Echo-completed destination compound plate using the Multidrop Combi (ThermoFisher Scientific, Waltham, MA). The compound

plate was shaken at 500 rpm for 5 minutes on a Teleshaker and then centrifuged at 1000 rpm for 1 min. 35 µL/well of the Glu EC_0 (Krebs buffer only), 5x EC_{80} (300 µM Glu), or 5x E_{MAX} (1 mM Glu) was loaded into the stimulus plate based on the plate map, using a multi-channel pipette.

The cell plate was washed on the BioTek ELX406 TS plate washer (Agilent) in three cycles with 80 µL/well/cycle of Krebs buffer, leaving residual volume of 20 µL/well. 20 µL/well of 1x dye loading solution was dispensed into the cell plate and incubated at room temperature for 45 min. After dye incubation, the buffer in the cell plate was aspirated down to 20 µL/well by ELX406 TS.

Panoptic tip box, cell plate, destination compound plate, and the glutamate stimulus plate were put into designated nests on Panoptic. The assay protocol was set with excitation at 517/20 nm, emission at 580/60 nm, gain at 1, and exposure 150 ms. After 124 seconds of baseline reading, 20 µL/well of 2x inhibitor was injected and read for 133 seconds (giving the basal membrane potential up to 257 seconds from the beginning of the assay) before the second injection of 10 µL/well of 5x glutamate from the stimulus plate and read continuously for an additional 607 seconds (giving the induced membrane potential). Fluorescent values were reduced using custom analysis software (Vanderbilt Waveguide) in a series of operations as follows: Fluorescent ratio calculated as values of the measurements over time divided by the initial fluorescent value at time 0. The maximum value during course of the EC_{80} (300µM) glutamate stimulation (257-700s) minus the minimum value 5 seconds before glutamate is added

(250-255s). This reduced value is normalized to the experimental plate mean response to 1mM glutamate representing the E_{MAX}. The percent maximum response of the concentration series of each test compound was fit using a 4PL model (GraphPad Prism) to estimate the potency reported as IC_{50}.

Intracellular L-Aspartate (L-Asp) uptake assay

HEK293 cells expressing the doxycycline-inducible SLC1A1 construct were seeded in 6-cm dishes (3.0E06 cells per dish). SLC1A1 expression was induced with doxycycline (150 ng/mL), with parallel non-induced controls. Concurrently, cells were treated overnight with Cmpd **3e**, PBJ1 or PBJ2 (10 µM). On the assay day, cells were washed once with PBS and incubated in glutamine-free DMEM supplemented with 2% dialyzed FBS and 1X Penicillin–Streptomycin for 3 h at 37°C. Cells were subsequently pulsed with L-Asp (100 µM) for 1.5 h at 37°C, maintaining the SLC1A1 inhibitors (10 µM) during starvation and adding aspartate.

Following the L-Asp pulse, cells were rinsed with normal saline (0.9% NaCl), and plates were immediately placed on dry ice. Samples were deproteinized by adding 1 mL ice-cold 80% (v/v) methanol (−80°C). Plates were incubated at −80°C for 20 min, scraped on dry ice, and lysates were transferred to microcentrifuge tubes. Samples were centrifuged at 14,000 × g for 5 min at 4 °C to remove debris. A total of 950 µL of the supernatant was transferred to fresh tubes and dried using a SpeedVac concentrator. Dried extracts were resuspended in 105 µL PBS.

Intracellular L-Asp was quantified using the EnzyChrom L-Aspartate Assay Kit (EASP-100; BioAssay Systems) according to the manufacturer's instructions. Briefly, 25 µL of each sample was loaded in duplicate into a 96-well plate together with L-Asp standards (0–400 µM). Sample blanks were prepared using working reagent lacking AST enzyme. Working reagent was prepared by combining Developer, AST enzyme, ODC enzyme, co-substrate, and dye reagent, and 75 µL was added per well. Plates were incubated for 60 min at 25°C protected from light, and absorbance was measured at 570 nm. L-Asp concentrations were determined from a standard curve after blank subtraction. The L-Asp levels in cells that were not treated by Dox were subtracted to calculate the amount of L-Asp in the presence or absence of the three inhibitors.

Drug combination assay and synergy analysis

For short-term (7 day) assays, A498 cells (1000 cells/well in a 96 well plate) were exposed to the HIF2α inhibitor PT2385 (0, 1, and 2 µM) in the presence of 10 µM of Cmpd **3e**, PBJ1, or PBJ2. At the end point, viable cell numbers were measured using CellTiter-Glo (Promega G9241). For the long-term (2-3 week) assays, A498 cells (200 cells per well in 12-well plates) were exposed to Cmpd **3e**, PBJ1, or PBJ2 (0, 1.5, 3, and 6 µM), each tested in combination with the HIF2α inhibitor PT2385 (0, 1, and 2 µM). Culture medium with fresh inhibitors was replenished every 3 days. At the end point, viable cell numbers were quantified using a Vi-Cell automated cell counter (Beckman Coulter). Cell viability was expressed relative to DMSO-treated controls. Experiments were performed as three independent biological replicates. Drug interaction was

evaluated using the SynergyFinder web application (RRID: SCR_019318) (Ianevski *et al.*, 2022) with the Bliss independence model and default settings.

Glutathione Detection

Glutathione measurements were done as per the manufacturer's instructions (Thermo Fisher Glutathione Colorimetric Detection Kit, Cat. # EIAGSHC). Briefly, A-498 cells (1.5E05 in a 10 cm dish) were treated with either Cmpd **3e**, PBJ1, or PBJ2 [each at 5 µM in 0.1 % (v/v) DMSO (vehicle control)] for 5 days. Cells were washed once with 1X PBS, trypsinized, and then harvested (300g, 5 min, 4 °C). Equal number of viable cells (5.0E05 per condition) were transferred to prechilled tubes, washed once in ice cold 1X PBS and immediately deproteinised in ice cold 5% sulfosalicylic acid (SSA). Cell lysates, generated by vortexing and sonication (3" pulse at 30% amplitude), were incubated on ice for 10 mins and then clarified (14,000xg, 10 min, 4°C). The supernatant was split into two pre-chilled tubes to measure total (GSH) and oxidized (GSSG) glutathione levels.

GSH samples were processed directly, whereas GSSG samples were treated with 2 vinylpyridine (2VP; 5 µL 2VP solution per 250 µL lysate) for 1 h at room temperature to derivatize free thiols and leave only oxidized glutathione. Both samples were first diluted 1:5 with Assay Buffer (final 1% SSA) and then another time at 1:4 with Sample Diluent buffer (final 1:20 dilution). 50 µL diluted samples were combined with 25 µL Colorimetric Detection Reagent and 25 µL Reaction Mixture (NADPH + glutathione reductase). Plates were mixed gently and incubated 20 min at room temperature, then

read at 405 nm on a SpectraMax i3 microplate reader. In parallel, a standard curve was generated for GSH (0–25 µM) and GSSG (0 - 12.5 µM) and used to calculate absolute concentrations of GSH and GSSG in the cell lysates.

Statistical Analysis

The sample sizes were determined based on prior experience working with these cell culture models. All experiments were typically repeated three (or more) times. One exception was the cytotoxicity screen, which was repeated twice because of the scale and cost of this experiment. The users were not blinded to the treatment groups. The statistical tests and sample sizes used in each experiment are outlined in the figure legends. Unless otherwise specified, the samples sizes indicate biological replicates. All tests were corrected for multiple testing, as necessary. Statistical significance was calculated using the Graphpad Prism software with appropriate corrections for multiple testing (as specified in the figure legends). Exact p-values were not reported below 0.0001 in this software, and these are marked as <0.0001[#] in our data.

Procedures for the Synthesis of Cmpd 3e and Analogs

General Scheme.

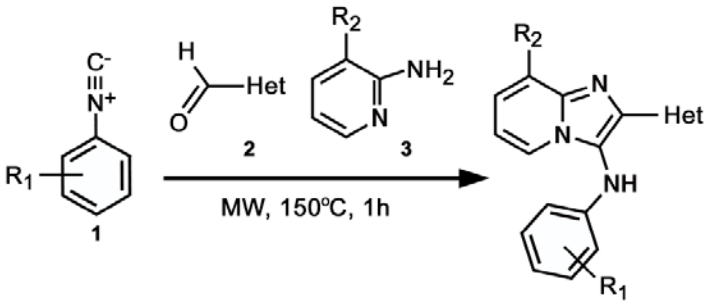

Synthesis of SLC1A1 (EAAT3) imidazopyridine cmpd **3e** and analogs reported herein were prepared according to the previously reported microwave irradiation protocol (Wu *et al.*, 2019). Procedures, characterization data, and purity are provided for compounds **4**, **10**, **12**, **14**, **30** (PBJ1), **38** (PBJ2). Additional analogs outside these compounds were prepared following a similar condensation microwave heating protocol, beginning with commercial or known isocyanides 1, aldehydes 2, and aminopyridines 3. The final imidazopyridines **1-38** had analytical purity >95% as judged by LC-MS and 1H NMR.

<u>8-Bromo-2-(1H-pyrazol-3-yl)-N-(o-tolyl)imidazo[1,2-a]pyridin-3-amine (4).</u>

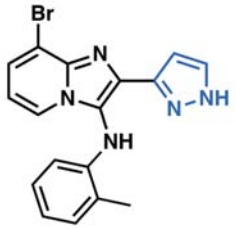

In a microwave reaction vial 1-isocyano-2-methylbenzene (102 mg, 0.87 mmol, 1.0 eq), 1*H*-pyrazole-3-carbaldehyde (84 mg, 0.87 mmol, 1.0 eq), and 3-bromopyridin-2-amine (150 mg, 0.87 mmol, 1.0 eq) were combined. The mixture was stirred neat at 160°C for 1 h under microwave radiation. The crude product was purified by silica gel chromatography to give 8-bromo-2-(1H-pyrazol-3-yl)-*N*-(*o*-tolyl)imidazo[1,2-*a*]pyridin-3-amine (51.3 mg, 16%) as yellow solid: LCMS (ESI): m/z = 368.0, $[M+H]^+$, R_t = 1.495 min; >95% (210, 254 nm); ^{1}H NMR (400 MHz, DMSO) δ 12.5 (m, 1H), 8.19 (s, 1H), 7.72 (d, J = 6.8 Hz, 1H), 7.50 (s, 1H), 7.14 (d, J = 6.8 Hz, 1H), 6.87 (dt, J = 14.5, 7.0 Hz, 2H), 6.69 (t, J = 7.4 Hz, 1H), 5.90 (d, J = 8.0 Hz, 1H), 2.40 (s, 3H).

<u>8-Bromo-2-(furan-2-yl)-*N*-(*m*-tolyl)imidazo[1,2-*a*]pyridin-3-amine (10).</u>

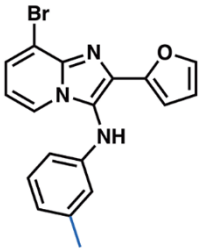

Step 1. Preparation of N-m-tolylformamide.

A mixture of 3-methoxyaniline (2 g, 18.7 mmol, 1 eq), formic acid (30 mL), and sodium formate (12.7 g, 186.6 mmol, 10 eq) in a 100 mL round-bottom flask was stirred with a magnetic stir bar at room temperature. The progress of the reaction was monitored by TLC. When the reaction reached completion, 30 mL of EtOAc was added into the system, and the organic solvent was then washed with H_2O (3 × 50 mL) and a saturated solution of $NaHCO_3$(50 mL). After drying with Na_2SO_4, the solvent was removed under reduced pressure. The resulting residue (890 mg, 35%) containing the *N-m*-tolylformamide was taken on to the next step without additional purification: LCMS (ESI): m/z = 152.0, $[M+H]^+$, R_t = 0.635 min; >90% (210, 254 nm).

Step 2. Preparation of 1-isocyano-3-methylbenzene.

To a solution of *N-m*-tolylformamide (800 mg, 5.92 mmol, 1 eq) and Et_3N (1.98 g, 19.53 mmol, 3.3 eq) in anhydrous DCM (10 mL) was added dropwise $POCl_3$ (998.2 mg, 6.51 mmol, 1.1 eq) at 0^oC under a nitrogen atmosphere over 35 min. Then the reaction mixture was stirred at 0^oC for 1 h. After completion, the reaction mixture was poured into a saturated solution of $NaHCO_3$ at 0^oC. The mixture was extracted by DCM. The organic phase was dried over Na_2SO_4 and the solvent was removed under reduced pressure. The crude product was purified by silica gel column chromatography to give the title

product as a yellow green liquid (600 mg, 86%) which was used directly in step 3 without further purification.

Step 3. Procedure for preparation of 8-bromo-2-(furan-2-yl)-N-(m-tolyl)imidazo[1,2-a]pyridin-3-amine.

To 1-isocyano-3-methylbenzene (203.1 mg, 1.73 mmol, 1.0 eq) from step 2, furan-2-carbaldehyde (166.6 mg,1.73 mmol, 1.0 eq), and 3-bromopyridin-2-amine (300 mg, 1.73 mmol, 1.0 eq) were mixed together in a microwave reaction vial. The mixture was stirred neat at 160°C for 1 h under microwave radiation. The crude product was purified by silica gel chromatography to give 8-bromo-2-(furan-2-yl)-*N*-(*m*-tolyl)imidazo[1,2-*a*]pyridin-3-amine (53.3 mg, 8%) as white solid: LCMS (ESI): m/z = 369.9, $[M+3H]^+$, R_t = 1.810 min; >90% (210, 254 nm); ^{1}H NMR (400 MHz, DMSO) δ 8.27 (s, 1H), 8.01 (d, J = 5.9 Hz, 1H), 7.76 (d, J = 1.0 Hz, 1H), 7.68 (d, J = 6.5 Hz, 1H), 7.03 (s, 1H), 6.88 (s, 1H), 6.71 (s, 1H), 6.58 (dd, J = 3.4, 1.8 Hz, 1H), 6.33 (dd, J = 8.0, 2.0 Hz, 1H), 6.09 (d, J = 2.1 Hz, 1H), 6.05 (d, J = 7.9 Hz, 1H), 3.63 (s, 3H).

<u>8-Bromo-*N*-(2-chlorophenyl)-2-(furan-2-yl)imidazo[1,2-*a*]pyridin-3-amine (12).</u>

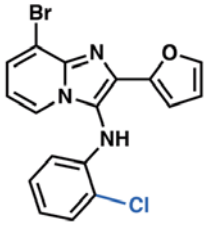

Step 1. Preparation of N-(2-chlorophenyl)formamide.

A mixture of 2-chloroaniline (3 g, 23.6 mmol, 1 eq), formic acid (30 mL), and sodium formate (1.6 g, 23 mmol, 1 eq) in a 50 mL round-bottom flask was stirred with a

magnetic stir bar at room temperature. The progress of the reaction was monitored by TLC. When the reaction finished, 30 mL of EtOAc was added into the system, and the organic solvent was then washed with H_2O (3 × 50 mL) and a saturated solution of $NaHCO_3$ (50mL). After drying with Na_2SO_4, the solvent was removed under reduced pressure. The resulting residue (2 g, 56%) containing the *N*-(2-chlorophenyl)formamide was taken on to the next step without further purification: LCMS (ESI): m/z = 156.1, $[M+H]^+$, R_t = 1.330 min; >95% (210, 254 nm).

Step 2. Preparation of 1-chloro-2-isocyanobenzene.

To a solution of N-(2-chlorophenyl)formamide (3.5 g, 22.5 mmol, 1 eq) and Et_3N (7.5 g, 74.5 mmol, 3.3 eq) in anhydrous DCM (40 mL) was added dropwise $POCl_3$ (3.8 g, 24.8 mmol, 1.1 eq) at 0^oC under a nitrogen atmosphere over 35 min. Then the reaction mixture was stirred at 0^oC for 1 h. After completion, the reaction mixture was poured onto a saturated solution of $NaHCO_3$ at 0^oC. The mixture was extracted by DCM. The organic phase was dried over Na_2SO_4 and the solvent was removed under reduced pressure. The crude product 1-chloro-2-isocyanobenzene was purified by silica gel column chromatography to give the product as a yellow green liquid (2.4 g, 80%). The isocyanide was used directly in step 3 without further purification.

Step 3. Preparation of 8-bromo-N-(2-chlorophenyl)-2-(furan-2-yl)imidazo[1,2-a]pyridin-3-amine.

To 1-chloro-2-isocyanobenzene (500 mg, 3.64 mmol, 1.0 eq) from step 2, furan-2-carbaldehyde (350 mg, 3.64 mmol, 1.0 eq), and 3-bromopyridin-2-amine (627 mg, 3.64

mmol, 1.0 eq) were mixed together in a microwave reaction vial. The mixture was heated neat at 160 ^{o}C for 1 h under microwave radiation. The crude product was purified by silica gel chromatography to give 8-bromo-*N*-(2-chlorophenyl)-2-(furan-2-yl)imidazo[1,2-a]pyridin-3-amine (45 mg, <5%) as white solid: LCMS (ESI): m/z = 389.8, $[M+H]^+$, R_t = 1.855 min; >95% (210, 254 nm); ^{1}H NMR (400 MHz, DMSO) δ 8.06 (d, J = 5.9 Hz, 1H), 7.98 (s, 1H), 7.74 (d, J = 1.1 Hz, 1H), 7.70 (d, J = 6.6 Hz, 1H), 7.42 (dd, J = 7.9, 1.4 Hz, 1H), 6.98 (s, 1H), 6.88 (t, J = 7.0 Hz, 1H), 6.77 (s, 1H), 6.63 (d, J = 3.3 Hz, 1H), 6.56 (dd, J = 3.3, 1.8 Hz, 1H), 6.11 (dd, J = 8.2, 1.4 Hz, 1H).

<u>8-Bromo-2-(furan-2-yl)-*N*-(3-methoxyphenyl)imidazo[1,2-*a*]pyridin-3-amine (14).</u>

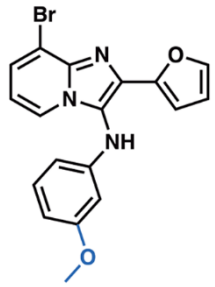

Step 1. Preparation of N-(3-methoxyphenyl)formamide.

A mixture of 3-methoxyaniline (3 g, 24.39 mmol, 1 eq), formic acid (30 mL), and sodium formate (16 g, 243.9 mmol, 10 eq) in a 50 mL round-bottom flask was stirred with a magnet at room temperature. The progress of the reaction was monitored by TLC. When the reaction finished, 30 mL of EtOAc was added into the system, and the organic solvent was then washed with H_2O (3 × 50 mL) and a saturated solution of $NaHCO_3$ (50 mL). After drying with Na_2SO_4, the solvent was removed under reduced pressure. The resulting residue (2.4 g, 15.89 mmol, 66.6 %) containing the *N*-(3-

methoxyphenyl)formamide was taken on to the next step without additional purification: LCMS (ESI): m/z = 152.0, $[M+H]^+$, R_t = 0.635 min; >95% (210, 254 nm).

Step 2. Preparation of starting material 1-isocyano-3-methoxybenzene.

To a solution of *N*-(3-methoxyphenyl)formamide (2.4 g, 15.8 mmol, 1 eq) and Et_3N (5.29 g, 52.4 mmol, 3.3 eq) in anhydrous DCM (40 mL) was added dropwise $POCl_3$ (2.67 g, 17.4 mmol, 1.1 eq) at 0°C under a nitrogen atmosphere over 35 min. Then the reaction mixture was stirred at 0°C for 1 h. After completion, the reaction mixture was poured into a saturated solution of $NaHCO_3$ at 0°C. Then the mixture was extracted by DCM. The organic phase was dried over Na_2SO_4, and the solvent was removed under reduced pressure. The crude product was purified by silica gel column chromatography to give the product as a yellow-green liquid (2.0 g, 95%). The isocyanide was used directly in step 3 without further purification.

Step 3. Preparation of 8-bromo-2-(furan-2-yl)-N-(3-methoxyphenyl)imidazo[1,2-a]pyridin-3-amine.

To a solution of 1-isocyano-3-methoxybenzene (200 mg, 1.5 mmol, 1.0 eq) from step 2 above, furan-2-carbaldehyde (144 mg,1.5 mmol, 1.0 eq), and 3-bromopyridin-2-amine (258 mg, 1.5 mmol, 1.0 eq) were combined in a microwave reaction vial. The mixture was heated neat at 160 ^{o}C for 1 h under microwave radiation with stirring. The crude product was purified by silica gel chromatography to give title compound 8-bromo-2-(furan-2-yl)-*N*-(3-methoxyphenyl)imidazo[1,2-a]pyridin-3-amine (40 mg, 7%) as a white solid: LCMS (ESI): m/z = 385.9, $[M+H+2]^+$, R_t = 1.557 min; >95% (210, 254 nm); ^{1}H

NMR (400 MHz, DMSO) δ 8.27 (s, 1H), 8.01 (d, J = 5.9 Hz, 1H), 7.76 (d, J = 1.0 Hz, 1H), 7.68 (d, J = 6.5 Hz, 1H), 7.03 (s, 1H), 6.88 (s, 1H), 6.71 (s, 1H), 6.58 (dd, J = 3.4, 1.8 Hz, 1H), 6.33 (dd, J = 8.0, 2.0 Hz, 1H), 6.09 (d, J = 2.1 Hz, 1H), 6.05 (d, J = 7.9 Hz, 1H), 3.63 (s, 3H).

<u>*Tert*-butyl 3-(8-bromo-7-fluoro-3-(o-tolylamino)imidazo[1,2-*a*]pyridin-2-yl)azetidine-1-carboxylate (PBJ1).</u>

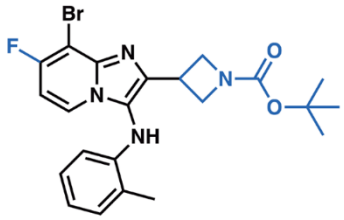

A mixture of 1-isocyano-2-methylbenzene (122.7 mg, 1.59 mmol, 1.05 eq), *tert*-butyl-3-formylazetidine-1-carboxylate (194 mg, 1.05 mmol, 1.0 eq), and 3-bromo-4-fluoropyridin-2-amine (200 mg, 1.05 mmol, 1.0 eq) was combined in a microwave reaction vial. The mixture was stirred at 160 °C for 1 h under microwave radiation. The crude product was purified by RP-HPLC to give the title compound (102.2 mg, 6%) as yellow solid: LCMS (ESI): m/z = 477.0, $[M+3H]^+$, R_t = 1.557 min; >95% (210, 254 nm); ^{1}H NMR (400 MHz, DMSO) δ 12.5 (m, 1H), 8.19 (s, 1H), 7.72 (d, J = 6.8 Hz, 1H), 7.50 (s, 1H), 7.14 (d, J = 6.8 Hz, 1H), 6.87 (dt, J = 14.5, 7.0 Hz, 2H), 6.69 (t, J = 7.4 Hz, 1H), 5.90 (d, J = 8.0 Hz, 1H), 2.40 (s, 3H).

<u>8-(Difluoromethyl)-2-(furan-2-yl)-*N*-(*o*-tolyl)imidazo[1,2-*a*]pyridin-3-amine (PBJ2).</u>

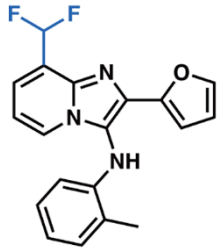

A mixture of 1-isocyano-2-methylbenzene (150 mg, 1.28 mmol), furan-2-carbaldehyde (123 mg, 1.28 mmol), and 3-(difluoromethyl)pyridin-2-amine (185 mg, 1.28 mmol) were combined in a microwave reaction vial and heated neat at 150 °C for 1 h under microwave radiation. After completion, the reaction was cooled and purified by flash chromatography (EtOAc/hexanes). The crude product containing fractions were concentrated and further purified by HPLC. The final product was isolated as a yellow solid to give 8-(difluoromethyl)-2-(furan-2-yl)-*N*-(*o*-tolyl)imidazo[1,2-*a*]pyridin-3-amine (34.79 mg, 8%): LCMS (ESI): m/z = 340.1, $[M+H]^+$, R_t = 1.35 min; >95% (210, 254 nm); ^{1}H NMR (400 MHz, DMSO) δ 8.14 (d, J = 6.6 Hz, 1H), 7.74 (s, 1H), 7.63 (s, 0.24H), 7.59 (d, J = 6.7 Hz, 1H), 7.49 (s, 1.5H), 7.36 (s, 0.26H), 7.15 (d, J = 7.3 Hz, 1H), 7.03 (t, J = 6.9 Hz, 1H), 6.84 (t, J = 7.6 Hz, 1H), 6.67 (t, J = 7.3 Hz, 1H), 6.62 (d, J = 3.2 Hz, 1H), 6.55 (dd, J = 3.3, 1.8 Hz, 1H), 5.87 (d, J = 7.9 Hz, 1H), 2.41 (s, 3H).

Data Availability

All the data necessary to evaluate the conclusions of the manuscript are provided in the paper and/or in the Appendix. The Cryo-EM maps and atomic coordinates have been deposited in the Electron Microscopy Data Bank (EMDB) and Protein Data Bank (PDB) under accession codes: EMD-71288 (https://www.ebi.ac.uk/emdb/EMD-71288, SLC1A1g protomer with **3e** and cholesterol, class A), corresponding to PDB-9P4X (https://www.rcsb.org/structure/9P4X); EMD-71289 (https://www.ebi.ac.uk/emdb/EMD-

71289, SLC1A1g protomer with **3e** and GDN, class B), corresponding to PDB-9P4Y (https://www.rcsb.org/structure/9P4Y); EMD-71290 (https://www.ebi.ac.uk/emdb/EMD-71290, Na^+-bound SLC1A1g protomer), corresponding to PDB-9P4Z (https://www.rcsb.org/structure/9P4Z); EMD-75048 (https://www.ebi.ac.uk/emdb/EMD-75048, SLC1A1 in the presence of 300 mM KCl and **3e**); and EMD-75049 (https://www.ebi.ac.uk/emdb/EMD-75049, SLC1A1 in the OF state in the presence of 300 mM KCl and **3e**).

Acknowledgments

We thank Carl Fluck at the Weill Cornell Medicine Electron Microscopy facility for the initial grid screening and preliminary data collection, and Robert Grassucci, Zhening Zhang, and Yen-hong Kao at Columbia University Cryo-Electron Microscopy Center for high-resolution data collection. NanoDSF experiments were performed on the Tycho NT.6 instrument in the Molecular Biophysics core facility at Weill Cornell Medicine under the leadership of Dr. Radda Rusinova. This work was supported by the following grants to AAC.: seed money from the Cleveland Clinic Foundation, the DoD KCRP-ECI award (W81XWH-20-1-0804), and the Velosano pilot award. Additionally, AAC, OB, and SRS were supported with a DoD-KCRP-IDA (HT9425-25-1-0761). PK was supported by a postdoctoral fellowship from Velosano. JAC, NSW, TR, CMG and SRS were supported by funds from Shared Laboratory Services at the Lerner Research Institute. OB was supported by HHMI and the National Institute of Neurological Disorders and Stroke (R37NS085318).

Disclosure Statement and Competing Interests

The authors declare no conflicts of interest with the work presented in this manuscript.

REFERENCES

Abrahamsen B, Schneider N, Erichsen MN, Huynh TH, Fahlke C, Bunch L, Jensen AA (2013) Allosteric modulation of an excitatory amino acid transporter: the subtype-selective inhibitor UCPH-101 exerts sustained inhibition of EAAT1 through an intramonomeric site in the trimerization domain. *J Neurosci* 33: 1068-1087

Adams PD, Afonine PV, Bunkoczi G, Chen VB, Davis IW, Echols N, Headd JJ, Hung LW, Kapral GJ, Grosse-Kunstleve RW *et al* (2010) PHENIX: a comprehensive Python-based system for macromolecular structure solution. *Acta Crystallogr D Biol Crystallogr* 66: 213-221

Alleva C, Kovalev K, Astashkin R, Berndt MI, Baeken C, Balandin T, Gordeliy V, Fahlke C, Machtens JP (2020) Na(+)-dependent gate dynamics and electrostatic attraction ensure substrate coupling in glutamate transporters. *Sci Adv* 6

Aoyama K, Matsumura N, Watabe M, Nakaki T (2008) Oxidative stress on EAAC1 is involved in MPTP-induced glutathione depletion and motor dysfunction. *Eur J Neurosci* 27: 20-30

Aoyama K, Suh SW, Hamby AM, Liu J, Chan WY, Chen Y, Swanson RA (2006) Neuronal glutathione deficiency and age-dependent neurodegeneration in the EAAC1 deficient mouse. *Nat Neurosci* 9: 119-126

Bailey CG, Ryan RM, Thoeng AD, Ng C, King K, Vanslambrouck JM, Auray-Blais C, Vandenberg RJ, Broer S, Rasko JE (2011) Loss-of-function mutations in the glutamate transporter SLC1A1 cause human dicarboxylic aminoaciduria. *The Journal of clinical investigation* 121: 446-453

Birsoy K, Wang T, Chen WW, Freinkman E, Abu-Remaileh M, Sabatini DM (2015) An Essential Role of the Mitochondrial Electron Transport Chain in Cell Proliferation Is to Enable Aspartate Synthesis. *Cell* 162: 540-551

Boudker O, Ryan RM, Yernool D, Shimamoto K, Gouaux E (2007) Coupling substrate and ion binding to extracellular gate of a sodium-dependent aspartate transporter. *Nature* 445: 387-393

Canul-Tec JC, Assal R, Cirri E, Legrand P, Brier S, Chamot-Rooke J, Reyes N (2017) Structure and allosteric inhibition of excitatory amino acid transporter 1. *Nature* 544: 446-451

Canul-Tec JC, Kumar A, Dhenin J, Assal R, Legrand P, Rey M, Chamot-Rooke J, Reyes N (2022) The ion-coupling mechanism of human excitatory amino acid transporters. *The EMBO journal* 41: e108341

Chen J, Cui L, Lu S, Xu S (2024) Amino acid metabolism in tumor biology and therapy. *Cell death & disease* 15: 42

Chen W, Hill H, Christie A, Kim MS, Holloman E, Pavia-Jimenez A, Homayoun F, Ma Y, Patel N, Yell P *et al* (2016) Targeting renal cell carcinoma with a HIF-2 antagonist. *Nature* 539: 112-117

Cho H, Du X, Rizzi JP, Liberzon E, Chakraborty AA, Gao W, Carvo I, Signoretti S, Bruick RK, Josey JA *et al* (2016) On-target efficacy of a HIF-2alpha antagonist in preclinical kidney cancer models. *Nature* 539: 107-111

Danbolt NC (2001) Glutamate uptake. *Prog Neurobiol* 65: 1-105

Danbolt NC, Furness DN, Zhou Y (2016) Neuronal vs glial glutamate uptake: Resolving the conundrum. *Neurochemistry international* 98: 29-45

Danbolt NC, Storm-Mathisen J, Kanner BI (1992) An [Na+ + K+]coupled L-glutamate transporter purified from rat brain is located in glial cell processes. *Neuroscience* 51: 295-310

Emsley P, Lohkamp B, Scott WG, Cowtan K (2010) Features and development of Coot. *Acta Crystallogr D Biol Crystallogr* 66: 486-501

Erichsen MN, Huynh TH, Abrahamsen B, Bastlund JF, Bundgaard C, Monrad O, Bekker-Jensen A, Nielsen CW, Frydenvang K, Jensen AA *et al* (2010) Structure-activity relationship study of first selective inhibitor of excitatory amino acid transporter subtype

1: 2-Amino-4-(4-methoxyphenyl)-7-(naphthalen-1-yl)-5-oxo-5,6,7,8-tetrahydro-4H-chromene-3-carbonitrile (UCPH-101). *J Med Chem* 53: 7180-7191

Focke PJ, Moenne-Loccoz P, Larsson HP (2011) Opposite movement of the external gate of a glutamate transporter homolog upon binding cotransported sodium compared with substrate. *J Neurosci* 31: 6255-6262

Gameiro PA, Yang J, Metelo AM, Perez-Carro R, Baker R, Wang Z, Arreola A, Rathmell WK, Olumi A, Lopez-Larrubia P *et al* (2013) In vivo HIF-mediated reductive carboxylation is regulated by citrate levels and sensitizes VHL-deficient cells to glutamine deprivation. *Cell Metab* 17: 372-385

Garcia-Bermudez J, Baudrier L, La K, Zhu XG, Fidelin J, Sviderskiy VO, Papagiannakopoulos T, Molina H, Snuderl M, Lewis CA *et al* (2018) Aspartate is a limiting metabolite for cancer cell proliferation under hypoxia and in tumours. *Nat Cell Biol* 20: 775-781

Goddard TD, Huang CC, Meng EC, Pettersen EF, Couch GS, Morris JH, Ferrin TE (2018) UCSF ChimeraX: Meeting modern challenges in visualization and analysis. *Protein science : a publication of the Protein Society* 27: 14-25

Gordan JD, Lal P, Dondeti VR, Letrero R, Parekh KN, Oquendo CE, Greenberg RA, Flaherty KT, Rathmell WK, Keith B *et al* (2008) HIF-alpha effects on c-Myc distinguish

two subtypes of sporadic VHL-deficient clear cell renal carcinoma. *Cancer Cell* 14: 435-446

Grewer C, Balani P, Weidenfeller C, Bartusel T, Tao Z, Rauen T (2005) Individual subunits of the glutamate transporter EAAC1 homotrimer function independently of each other. *Biochemistry* 44: 11913-11923

Grewer C, Gameiro A, Rauen T (2014) SLC1 glutamate transporters. *Pflugers Arch* 466: 3-24

Grubb T, Koochaki P, Matar S, Ghandour F, Machaalani M, Saad E, Tang C, Reznik E, Khatun J, Salem C *et al* (2025) The SLC1A1/EAAT3 dicarboxylic amino acid transporter is an epigenetically dysregulated nutrient carrier that sustains oncogenic metabolic programs. *Nature communications* 16: 10012

Guo W, Li K, Sun B, Xu D, Tong L, Yin H, Liao Y, Song H, Wang T, Jing B *et al* (2021) Dysregulated Glutamate Transporter SLC1A1 Propels Cystine Uptake via Xc(-) for Glutathione Synthesis in Lung Cancer. *Cancer Res* 81: 552-566

Hediger MA, Clemencon B, Burrier RE, Bruford EA (2013) The ABCs of membrane transporters in health and disease (SLC series): introduction. *Mol Aspects Med* 34: 95-107

Himi T, Ikeda M, Yasuhara T, Nishida M, Morita I (2003) Role of neuronal glutamate transporter in the cysteine uptake and intracellular glutathione levels in cultured cortical neurons. *J Neural Transm (Vienna)* 110: 1337-1348

Ianevski A, Giri AK, Aittokallio T (2022) SynergyFinder 3.0: an interactive analysis and consensus interpretation of multi-drug synergies across multiple samples. *Nucleic acids research* 50: W739-W743

Jonasch E, Donskov F, Iliopoulos O, Rathmell WK, Narayan VK, Maughan BL, Oudard S, Else T, Maranchie JK, Welsh SJ *et al* (2021) Belzutifan for Renal Cell Carcinoma in von Hippel-Lindau Disease. *N Engl J Med* 385: 2036-2046

Kanai Y, Clemencon B, Simonin A, Leuenberger M, Lochner M, Weisstanner M, Hediger MA (2013) The SLC1 high-affinity glutamate and neutral amino acid transporter family. *Mol Aspects Med* 34: 108-120

Kanai Y, Hediger MA (1992) Primary structure and functional characterization of a high-affinity glutamate transporter. *Nature* 360: 467-471

Kato T, Kusakizako T, Jin C, Zhou X, Ohgaki R, Quan L, Xu M, Okuda S, Kobayashi K, Yamashita K *et al* (2022) Structural insights into inhibitory mechanism of human excitatory amino acid transporter EAAT2. *Nat Commun* 13: 4714

Koch HP, Brown RL, Larsson HP (2007) The glutamate-activated anion conductance in excitatory amino acid transporters is gated independently by the individual subunits. *J Neurosci* 27: 2943-2947

Kondo K, Kim WY, Lechpammer M, Kaelin WG, Jr. (2003) Inhibition of HIF2alpha is sufficient to suppress pVHL-defective tumor growth. *PLoS biology* 1: E83

Kortzak D, Alleva C, Weyand I, Ewers D, Zimmermann MI, Franzen A, Machtens JP, Fahlke C (2019) Allosteric gate modulation confers K(+) coupling in glutamate transporters. *The EMBO journal* 38: e101468

Leary GP, Stone EF, Holley DC, Kavanaugh MP (2007) The glutamate and chloride permeation pathways are colocalized in individual neuronal glutamate transporter subunits. *J Neurosci* 27: 2938-2942

Lin L, Yee SW, Kim RB, Giacomini KM (2015) SLC transporters as therapeutic targets: emerging opportunities. *Nat Rev Drug Discov* 14: 543-560

Ling ZN, Jiang YF, Ru JN, Lu JH, Ding B, Wu J (2023) Amino acid metabolism in health and disease. *Signal Transduct Target Ther* 8: 345

Mitchell TJ, Turajlic S, Rowan A, Nicol D, Farmery JHR, O'Brien T, Martincorena I, Tarpey P, Angelopoulos N, Yates LR *et al* (2018) Timing the Landmark Events in the Evolution of Clear Cell Renal Cell Cancer: TRACERx Renal. *Cell* 173: 611-623 e617

Palos TP, Ramachandran B, Boado R, Howard BD (1996) Rat C6 and human astrocytic tumor cells express a neuronal type of glutamate transporter. *Brain Res Mol Brain Res* 37: 297-303

Peghini P, Janzen J, Stoffel W (1997) Glutamate transporter EAAC-1-deficient mice develop dicarboxylic aminoaciduria and behavioral abnormalities but no neurodegeneration. *The EMBO journal* 16: 3822-3832

Punjani A, Rubinstein JL, Fleet DJ, Brubaker MA (2017) cryoSPARC: algorithms for rapid unsupervised cryo-EM structure determination. *Nature methods* 14: 290-296

Qiu B, Boudker O (2023) Symport and antiport mechanisms of human glutamate transporters. *Nat Commun* 14: 2579

Qiu B, Boudker O (2025) Structural basis of excitatory amino acid transporter 3 substrate recognition. *Proc Natl Acad Sci U S A* 122: e2501627122

Qiu B, Matthies D, Fortea E, Yu Z, Boudker O (2021) Cryo-EM structures of excitatory amino acid transporter 3 visualize coupled substrate, sodium, and proton binding and transport. *Sci Adv* 7

Reyes N, Ginter C, Boudker O (2009) Transport mechanism of a bacterial homologue of glutamate transporters. *Nature* 462: 880-885

Ricketts CJ, De Cubas AA, Fan H, Smith CC, Lang M, Reznik E, Bowlby R, Gibb EA, Akbani R, Beroukhim R *et al* (2018) The Cancer Genome Atlas Comprehensive Molecular Characterization of Renal Cell Carcinoma. *Cell Rep* 23: 313-326 e315

Riederer EA, Moenne-Loccoz P, Valiyaveetil FI (2022) Distinct roles of the Na(+) binding sites in the allosteric coupling mechanism of the glutamate transporter homolog, Glt(Ph). *Proc Natl Acad Sci U S A* 119: e2121653119

Scheres SH (2012) RELION: implementation of a Bayesian approach to cryo-EM structure determination. *J Struct Biol* 180: 519-530

Shimamoto K, Lebrun B, Yasuda-Kamatani Y, Sakaitani M, Shigeri Y, Yumoto N, Nakajima T (1998) DL-threo-beta-benzyloxyaspartate, a potent blocker of excitatory amino acid transporters. *Mol Pharmacol* 53: 195-201

Shimamoto K, Sakai R, Takaoka K, Yumoto N, Nakajima T, Amara SG, Shigeri Y (2004) Characterization of novel L-threo-beta-benzyloxyaspartate derivatives, potent blockers of the glutamate transporters. *Mol Pharmacol* 65: 1008-1015

Shirole NH, Kesar D, Lee Y, Goodale A, Syamala S, Kukreja S, Li R, Qiu X, Yu W, Goldman S *et al* (2025) Requirement for Cyclin D1 Underlies Cell-Autonomous HIF2 Dependence in Kidney Cancer. *Cancer Discov* 15: 1484-1504

Sijben HJ, Dall' Acqua L, Liu R, Jarret A, Christodoulaki E, Onstein S, Wolf G, Verburgt SJ, Le Devedec SE, Wiedmer T *et al* (2022) Impedance-Based Phenotypic Readout of Transporter Function: A Case for Glutamate Transporters. *Front Pharmacol* 13: 872335

Sullivan LB, Gui DY, Hosios AM, Bush LN, Freinkman E, Vander Heiden MG (2015) Supporting Aspartate Biosynthesis Is an Essential Function of Respiration in Proliferating Cells. *Cell* 162: 552-563

Suloway C, Pulokas J, Fellmann D, Cheng A, Guerra F, Quispe J, Stagg S, Potter CS, Carragher B (2005) Automated molecular microscopy: the new Leginon system. *J Struct Biol* 151: 41-60

Turajlic S, Xu H, Litchfield K, Rowan A, Horswell S, Chambers T, O'Brien T, Lopez JI, Watkins TBK, Nicol D *et al* (2018) Deterministic Evolutionary Trajectories Influence Primary Tumor Growth: TRACERx Renal. *Cell* 173: 595-610 e511

Vandenberg RJ, Ryan RM (2013) Mechanisms of glutamate transport. *Physiol Rev* 93: 1621-1657

Verdon G, Oh S, Serio RN, Boudker O (2014) Coupled ion binding and structural transitions along the transport cycle of glutamate transporters. *eLife* 3: e02283

Wallace EM, Rizzi JP, Han G, Wehn PM, Cao Z, Du X, Cheng T, Czerwinski RM, Dixon DD, Goggin BS *et al* (2016) A Small-Molecule Antagonist of HIF2alpha Is Efficacious in Preclinical Models of Renal Cell Carcinoma. *Cancer Res* 76: 5491-5500

Wang J, Zhang K, Goyal P, Grewer C (2020) Mechanism and potential sites of potassium interaction with glutamate transporters. *J Gen Physiol* 152

Wang J, Zielewicz L, Grewer C (2019) A K(+)/Na(+) co-binding state: Simultaneous versus competitive binding of K(+) and Na(+) to glutamate transporters. *The Journal of biological chemistry* 294: 12180-12190

Watts SD, Torres-Salazar D, Divito CB, Amara SG (2014) Cysteine transport through excitatory amino acid transporter 3 (EAAT3). *PloS one* 9: e109245

Wen D, Li W, Song X, Hu M, Liao Y, Xu D, Deng J, Guo W (2025) NF-kappaB-mediated EAAT3 upregulation in antioxidant defense and ferroptosis sensitivity in lung cancer. *Cell death & disease* 16: 124

Wu P, Bjorn-Yoshimoto WE, Staudt M, Jensen AA, Bunch L (2019) Identification and Structure-Activity Relationship Study of Imidazo[1,2-a]pyridine-3-amines as First Selective Inhibitors of Excitatory Amino Acid Transporter Subtype 3 (EAAT3). *ACS Chem Neurosci* 10: 4414-4429

Xiong J, Wang N, Zhong HJ, Cui BW, Cheng S, Sun R, Chen JY, Xu PP, Cai G, Wang L *et al* (2021) SLC1A1 mediated glutamine addiction and contributed to natural killer T-cell lymphoma progression with immunotherapeutic potential. *EBioMedicine* 72: 103614

Yang Z, Su W, Wei X, Qu S, Zhao D, Zhou J, Wang Y, Guan Q, Qin C, Xiang J *et al* (2023) HIF-1alpha drives resistance to ferroptosis in solid tumors by promoting lactate production and activating SLC1A1. *Cell Rep* 42: 112945

Zerangue N, Kavanaugh MP (1996) Flux coupling in a neuronal glutamate transporter. *Nature* 383: 634-637

Zhang Z, Chen H, Geng Z, Yu Z, Li H, Dong Y, Zhang H, Huang Z, Jiang J, Zhao Y (2022) Structural basis of ligand binding modes of human EAAT2. *Nat Commun* 13: 3329

FIGURE LEGENDS

Figure 1. Compound 3e binds to *apo* inward-facing SLC1A1g protomers. (**A**) The transport cycle of SLC1A1 transporters. Outward-facing (OF) carriers bind substrate and symported ions under occluding HP2 (raspberry); the transport domain (blue) translocates relative to the stationary scaffold domain (white) into the inward-facing (IF) state, where it releases the substrate and ions; the transport domain returns into the OF state after binding a K^+ ion. Key ion and substrate-binding arginine (R) and glutamate (E) residues are shown for reference. (**B, C**) The surface representation of structures of Na^+-bound SLC1A1g observed in the cryo-EM sample **(B**) and the *apo* transporter (**C**, PDB access code 6X3F) in IF. The structures show an enlarged drug-binding pocket in the *apo* carrier. The scaffold domain is colored white, the transport domain is in various colors, and the residues within 4 Å of **3e** in the drug-bound states are colored in tan. The dotted gray lines represent the approximate boundaries of the membrane bilayer. (**D, E**). Structures of SLC1A1g bound to **3e** as seen in the structural classes A (**D**) and B (**E**). The compound **3e** is shown as spheres and colored orange. The EM density contoured at 5σ around the modeled **3e** is shown below the panels. (**F**) Thermal stabilization (mean ± S.D., n=5) of SLC1A1g by 100 µM **3e** in the presence and absence of 200 mM Na^+ (**G**) Thermal shifts induced by increasing Na^+ concentrations, as indicated, in the presence of the indicated concentrations of compound **3e** (mean ± S.D., n=6). The Tm measured at 0 mM NaCl was normalized to zero to demonstrate change in thermal stabilization.

Figure 2. Compound 3e and Na^+ ions compete for binding to SLC1A1g. (**A-D**) Structures of the *apo* SLC1A1g transport domain bound to **3e** (**A**). Modeled **3e** bound to SLC1A1g with Na^+ only (**B**), Na^+ and L-Glu (**C**), and with K^+ (**D**). The transport domain is depicted as a gray cartoon, with HP2 and TM3 highlighted in raspberry and green-cyan, respectively. L-Glu is depicted in blue, and Na^+ and the K^+ ions in purple. **3e** is shown as an orange surface where it is observed in cryo-EM (**C**) or modeled at corresponding positions (**B-D**). Modeling shows that in Na^+-bound transporter, with or without Glu, the compound would sterically clash with HP2. The binding pocket is preserved in the K^+-bound transporter. (**E, F**) Close-up view of the Na3 and **3e** binding sites in Na^+- and **3e**-bound states of SLC1A1g, respectively. Residues coordinating Na3 are shown as sticks. T102 coordinates Na3 (**E**) and, via a water-mediated hydrogen bond, **3e** (**F**). (**G**) An EM density map contoured at 5σ around the modeled side chains and waters in **3e-**bound SLC1A1g in the B structural class. (**H, I**) Structures of SLC1A1g bound to **3e** with cholesterol in structural class A (Cho, **H**) and GDN in class B (**I**) sandwiched between the drug and the scaffold domain. Scaffold and transport domains are shown in surface and cartoon representations, respectively. The TM2-TM3 loop colored light green. The EM density around **3e**, cholesterol, and GDN is contoured at 5σ and colored orange, teal, and slate blue, respectively. (**C**) Structure of SLC1A3/EAAT1 in OF state bound to UCPH-101 (PDB code 5LM4). The drug is colored pink and shown in surface representation. Note that UCPH-101 is more inwardly positioned than **3e** and coordinated by the cytoplasmic end of TM3.

Figure 3. Binding selectivity determinants and SLC1A1 drug-resistant mutants. (**A**) A close-up view of the **3e** binding pocket in cartoon and transparent surface representation. The SLC1A1 residues within 4 Å are shown as sticks and labeled in black. The **3e** backbone is numbered, and key functional groups are labeled in blue. Hydrogen bonds with the resolved water molecule (red) are shown as dashed lines. (**B**) Sequence alignment around TM3 residue F99 and HP2 residue T402 for SLC1 proteins. T402 is conserved while F99 is variable (**C**) Crystal violet staining of A498 cells that were lentivirally transduced to express sgRNA (sg5)-resistant versions of either wild-type (WT) or mutant SLC1A1, or GFP (as a control), and then transduced with sgRNA constructs to inactivate SLC1A1 (1A1sg5) or a non-targeting control (sgCon). (**D**) Viable cell number of isogenic A498 cells expressing the indicated forms of SLC1A1 (or GFP control) and then cultured in the presence of the indicated concentrations of **3e** for 20 days. Cell numbers, relative to vehicle DMSO treatment (blue dashed line), were represented as mean ± S.D., n=4, and compared to the GFP arm using two-way ANOVA with Tukey's multiple comparison test. P-values at 6 μM – WT: 0.97, FA: 0.98, FL: 0.02*, FM: 0.0002$^{\wedge}$, TI: 0.0021**, TL: 0.0004$^{\wedge}$. P-values at 12 μM – WT: 0.96, FA: 0.99, FL: 0.026*, FM: 0.0004$^{\wedge}$, TI: 0.0021**, TL: <0.0001$^{\#}$. (**E**) NanoDSF results showing changes in *Ti* for WT SLC1A1g versus the F99L and F99M mutants that lose the ability to bind **3e**. Experiments were repeated using two independent protein preparations with at least three technical repeats each and compared using one-way ANOVA with Dunnett's multiple comparison test, $^{\#}p<0.0001$.

Figure 4. Screening identifies novel BIA inhibitors. (**A**) Screening of **3e** analogs in thermal shift NanoDSF assays. Gray, yellow, and salmon regions represent, respectively, controls, compounds that stabilize SLC1A1g by more than 1°C, suggesting binding, and compounds that do not significantly stabilize SLC1A1g, suggesting they do not bind. No data were obtained for compounds interfering with fluorescence measurements (e.g., **40** and **41**). Results are averages of at least two independent biological repeats, each comprising at least three technical repeats. The box plots representing all points from the minima to maxima, interquartile range from 25th to 75th percentile, and median central line is shown. (**B**) Screening of **3e** analogs in high-throughput cytotoxicity assay using kidney cancer A498 cells. Mean IC_{50} values from two independent experiments are shown as blue columns and compared to **3e** control (red column). Selected compounds are colored green. (**C, D**) Chemical structure of the parental **3e** (**C**) and selected BIA compounds (**D**). Inhibitor **14** (red) is a highly cytotoxic off-target compound.

Figure 5. The antiproliferative properties of novel BIA compounds are on-target. (**A**-**C**) Dose-dependent cytotoxic effects of the parental **3e** and the novel PBJ1 and PBJ2 molecules on UMRC2 (**A**) and 786O (**B**) kidney cancer cells with fitted IC_{50} values (**C**). (**D**) PBJ1 and PBJ2 docked into the **3e** binding site. (**E**) Fold change in cell number, relative to vehicle DMSO treatment (blue dashed line), in A498 cells that were lentivirally transduced to expressing the indicated WT or drug-resistant mutants of SLC1A1 mutants, or GFP control, and then cultured in the presence of the indicated concentrations of PBJ1 or PBJ2 for 14-20 days. Data normalized to the DMSO arm was

plotted as mean ± S.D., n=3, and statistically compared to the GFP arm by two-way ANOVA adjusted using Tukey's multiple comparison test. P-values for PBJ1, at 1.5 μM – WT: 0.99^{ns}, FM: 0.0002$^{\wedge}$, TI: 0.0044**; at 3.0 μM – WT: 0.98^{ns}, FM: 0.0001$^{\#}$, TI: <0.0001$^{\#}$; at 6.0 μM – WT: 0.56^{ns}, FM: <0.0001$^{\#}$, TI: 0.0137*. P-values for PBJ2, at 1.5 μM – WT: 0.84^{ns}, FM: 0.0017**, TI: 0.0237*; at 3.0 μM – WT: 0.87^{ns}, FM: <0.0001$^{\#}$, TI: 0.0001$^{\#}$; at 6.0 μM – WT: 0.99^{ns}, FM: 0.0013**, TI: <0.0001$^{\#}$. ns = not significant. (**F**-**H**) Fold change (FC) in cell number relative to vehicle DMSO treatment (purple dashed line at 1.0) in A498 cells that were treated with the indicated combination doses of the HIF2 inhibitor, PT2385, and the SLC1A1 inhibitors, compound 3e (**F**), PBJ1 (**G**), or PBJ2 (**H**). Data normalized to the DMSO arm (grey bars), n=2, mean ± S.D., was statistically compared using two-way ANOVA with Dunnett's multiple comparison test. P-values in (**F**) at 0 μM PT2385 – 1.5: 0.16^{ns}, 3.0: 0.027*, 6.0: 0.0051**; 1 μM PT2385 – 1.5: 0.14^{ns}, 3.0: 0.0019**, 6.0: 0.001$^{\wedge}$; 2 μM PT2385 – 1.5: 0.86^{ns}, 3.0: 0.0708^{ns}, 6.0: 0.003**; ns = not significant. P-values in (**G**) at 0 μM PT2385 – 1.5: 0.0696^{ns}, 3.0: 0.0128*, 6.0: 0.0019**; 1 μM PT2385 – 1.5: 0.602^{ns}, 3.0: 0.0164*, 6.0: 0.0002$^{\wedge}$; 2 μM PT2385 – 1.5: 0.0044**, 3.0: 0.0006$^{\wedge}$, 6.0: 0.0003$^{\wedge}$; ns = not significant. P-values in (**H**) at 0 μM PT2385 – 1.5: <0.0001$^{\#}$, 3.0: <0.0001$^{\#}$, 6.0: <0.0001$^{\#}$; 1 μM PT2385 – 1.5: <0.0001$^{\#}$, 3.0: <0.0001$^{\#}$, 6.0: <0.0001$^{\#}$; 2 μM PT2385 – 1.5: <0.0001$^{\#}$, 3.0: <0.0001$^{\#}$, 6.0: <0.0001$^{\#}$. (**I-K**) Bliss synergy scores plotted using data in (F) to (H), for combination doses of the HIF2 inhibitor, PT2385, and the SLC1A1 inhibitors, compound 3e (**I**), PBJ1 (**J**), or PBJ2 (**K**).

Figure 6. Novel antiproliferative BIA compounds inhibit transport by SLC1A1. (**A**) Experimental design of the impedance assay. (**B**) Western blot showing SLC1

expression in HEK293 cells stably transfected with FLAG-tagged Dox-inducible versions of human *SLC1A1*, *SLC1A2*, and *SLC1A3* genes. (**C**) Time-dependent impedance increases in HEK293 cells expressing SLC1A1 in the presence of 1 mM L-Glu and increasing concentrations of **3e**. Data represents mean ± S.D. from two independent replicates. (**D**) Dose-dependent inhibition of impedance as measured by changes in integrated Area Under the Curve (AUC) upon treatment of cells in (**B**) and (**C**) with the indicated BIA compounds or **3e** and TFB-TBOA as controls. (**E**, **F**) Schema of the FLIPR based membrane potential assay measuring SLC1A1 activity (**E**) and changes in membrane potential triggered by SLC1A1-dependent Glu uptake measured using FLIPR in the presence of the indicated concentrations of **3e**, PBJ1, and PBJ2, represented as mean ± S.D., n=12 (**F**).

Figure 7. BIA compounds cause metabolic vulnerabilities in cancer cells. (**A**) SLC1A1 uptakes Asp, Glu, and Cys amino acids, which are necessary for the synthesis of nucleotides (NTPs), enter the TCA cycle, and are precursors of glutathione (GSH) biosynthesis. (**B**, **C**) Schema for measurement of SLC1A1-dependent uptake of Asp (**B**) and intracellular Asp levels (mean ± S.D., n=4) measured using a colorimetric assay kit (**C**) in HEK293 cells expressing Dox-inducible SLC1A1 (as described in Fig. 6B). Data compared to the DMSO arm using one-way ANOVA with Dunnett's multiple comparison test. P-values: 3e: 0.0078^{**}, PBJ1: 0.0003^{***}, PBJ2: 0.0003^{***} (**D**-**F**) Intracellular levels of reduced glutathione (GSH) (**D**) or oxidized glutathione (GSSG) (**E**), and changes in cell number (**F**), in A498 cells that were treated with 5 μM of the indicated compounds, or DMSO control. Data plotted as mean ± S.D., n=3, was statistically compared to the

DMSO arm by two-way ANOVA adjusted using Dunnett's multiple comparison test. P-values in (**D**): 3e: 0.0147*, PBJ1: <0.0001$^{\#}$, PBJ2: 0.0011**. P-values in (**E**): 3e: <0.0001$^{\#}$, PBJ1: <0.0001$^{\#}$, PBJ2: <0.0001$^{\#}$. P-values in (**F**): 3e: 0.0091**, PBJ1: <0.0001$^{\#}$, PBJ2: <0.0001$^{\#}$. (**G**-**I**) Cell counts measured using ViCell upon treatment with PBJ1 (**G**) or PBJ2 (**H**), and representative plates stained using crystal violet (**I**), in A498 cells that were grown in the presence of the indicated concentrations of PBJ1 or PBJ2, along with no treatment (Unt), 100 μM membrane-permeable methyl esters of L-Asp and L-Glu (meAsp, meGlu), or 1 mM GSH, as indicated, for 14-20 days. In (**G**) and (**H**), data plotted as mean ± S.D., n=3, was statistically compared to the same drug concentration in the Untreated (Unt) arm by two-ANOVA adjusted using Dunnett's multiple comparison test. P-values in (**G**) for the meAsp arm –1.5: 0.0048**, 3.0: <0.0001$^{\#}$, 6.0: 0.0001$^{\#}$; for the meGlu arm – 1.5: 0.2349^{ns}, 3.0: <0.0025**, 6.0: 0.0259*; for the GSH arm – 1.5: 0.0109*, 3.0: <0.0001$^{\#}$, 6.0: 0.0008$^{\wedge}$. P-values in (**H**) for the meAsp arm –1.5: 0.0020**, 3.0: <0.0008$^{\wedge}$, 6.0: <0.0001$^{\#}$; for the meGlu arm – 1.5: 0.0512^{ns}, 3.0: 0.0992^{ns}, 6.0: 0.0006$^{\wedge}$; for the GSH arm – 1.5: 0.0017**, 3.0: 0.0007$^{\wedge}$, 6.0: <0.0001$^{\#}$.

Table 1

Mutagenesis Primers		
Name	Mutation	Sequence
1A1F99Atop	F99A	GCTGTCGTGTATTATGCCTGTACCACTCTCATT
1A1F99Abtm	F99A	AATGAGAGTGGTACAGGCATAATACACGACAGC
1A1F99Mtop	F99M	GCTGTCGTGTATTATATGTGTACCACTCTCATT
1A1F99Mbtm	F99M	AATGAGAGTGGTACACATATAATACACGACAGC
1A1F99Ltop	F99L	GCTGTCGTGTATTATTTATGTACCACTCTCATT
1A1F99Lbtm	F99L	AATGAGAGTGGTACATAAATAATACACGACAGC
1A1T402Itop	T402I	ATCAGTATCACGGCCATATCTGCCAGCATCGGA
1A1T402Ibtm	T402I	TCCGATGCTGGCAGATATGGCCGTGATACTGAT
1A1T402Ltop	T402L	ATCAGTATCACGGCCTTATCTGCCAGCATCGGA
1A1T402Lbtm	T402L	TCCGATGCTGGCAGATAAGGCCGTGATACTGAT
Cloning (sgRNA) sequences		
Name	Target	Sequence
CT110 (sgCon)	Non-Targeting	GGAGGCTAAGCGTCGCAA
1A1sg5	*SLC1A1*	TCACCTGATGAGATCTAACA

FIGURE 1

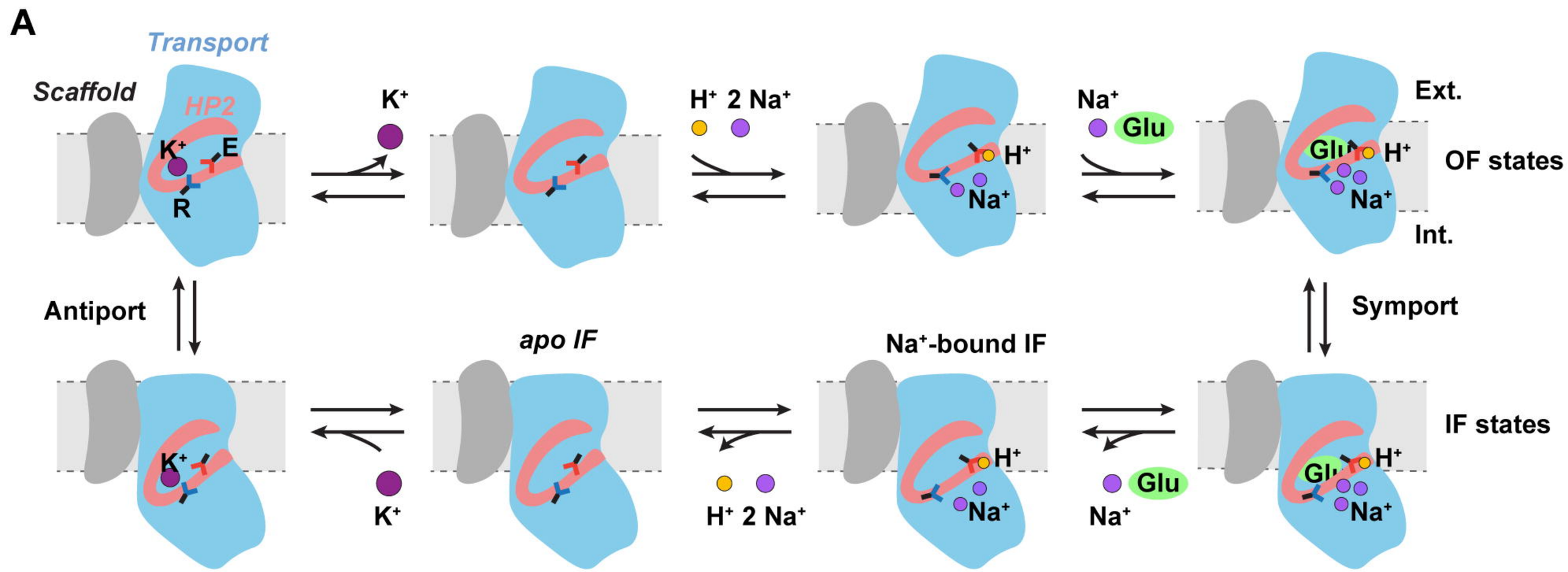

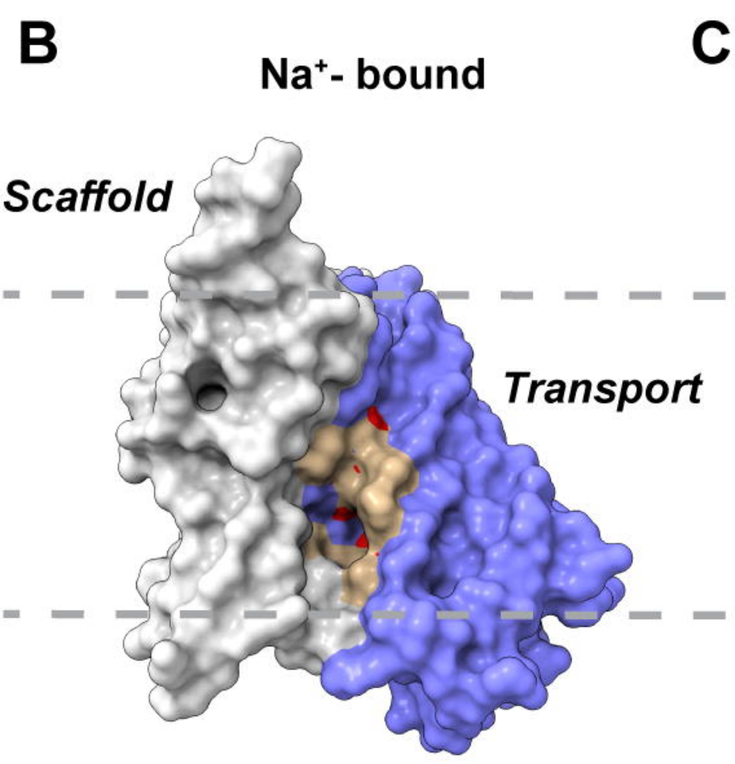

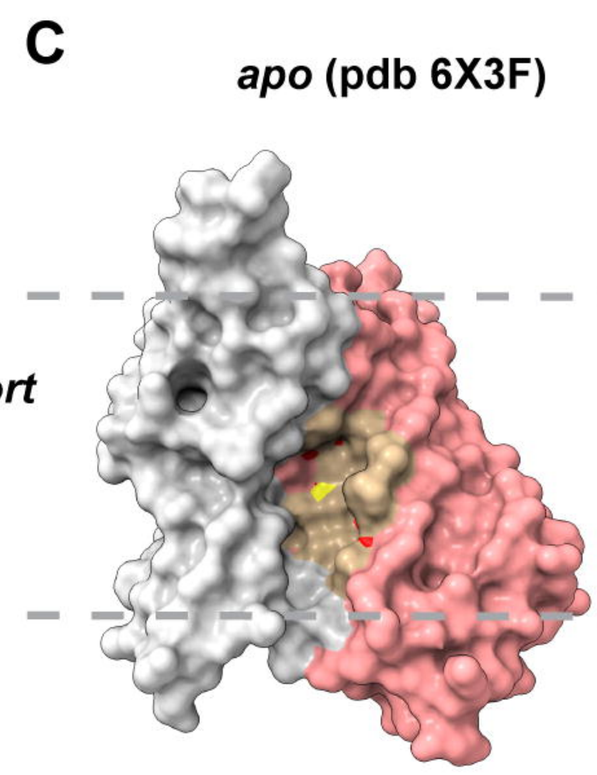

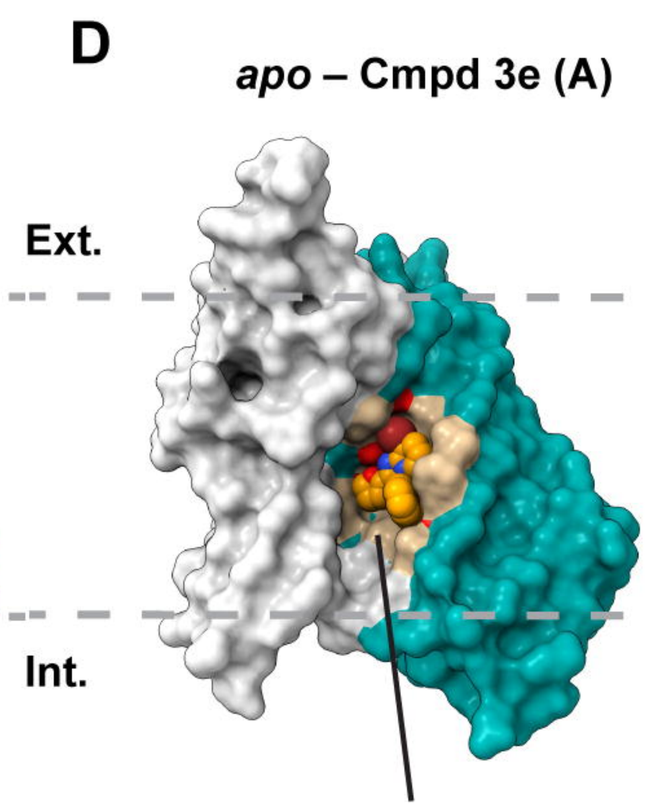

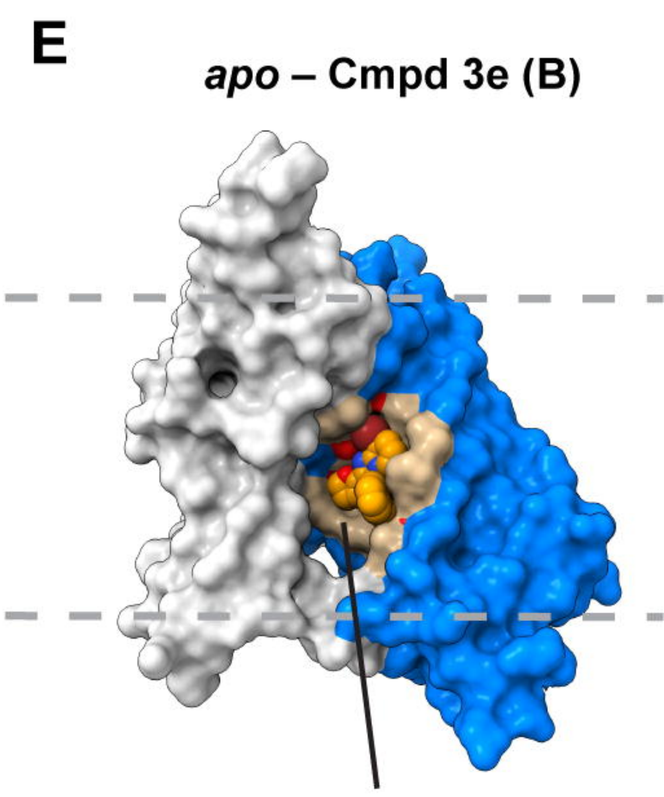

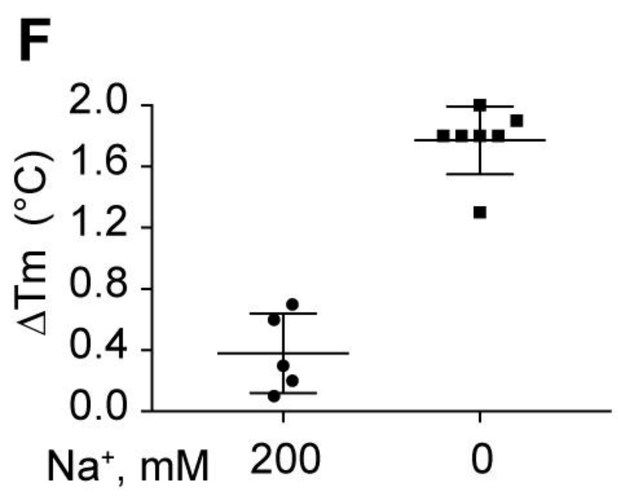

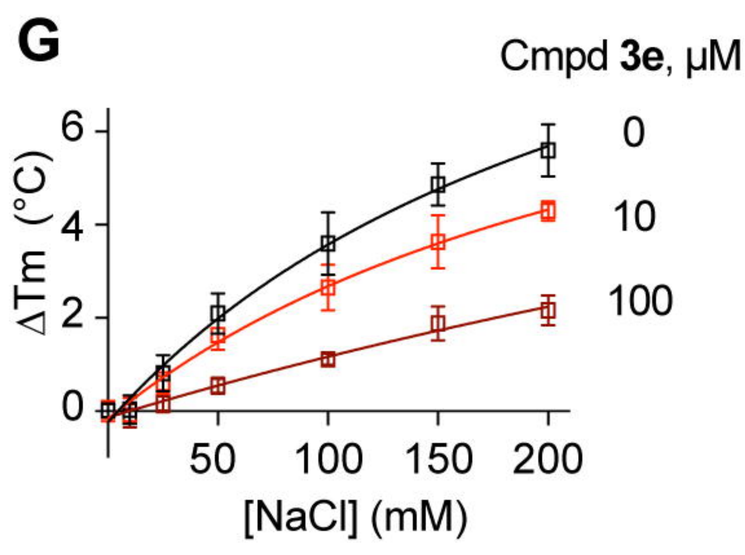

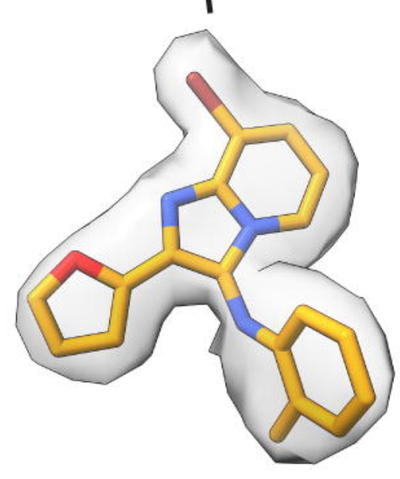

Cmpd 3e (A) map

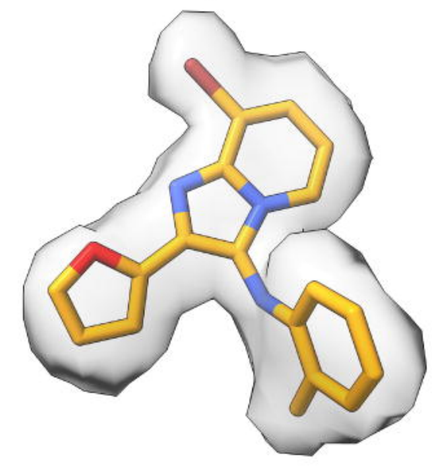

Cmpd 3e (B) map

FIGURE 2

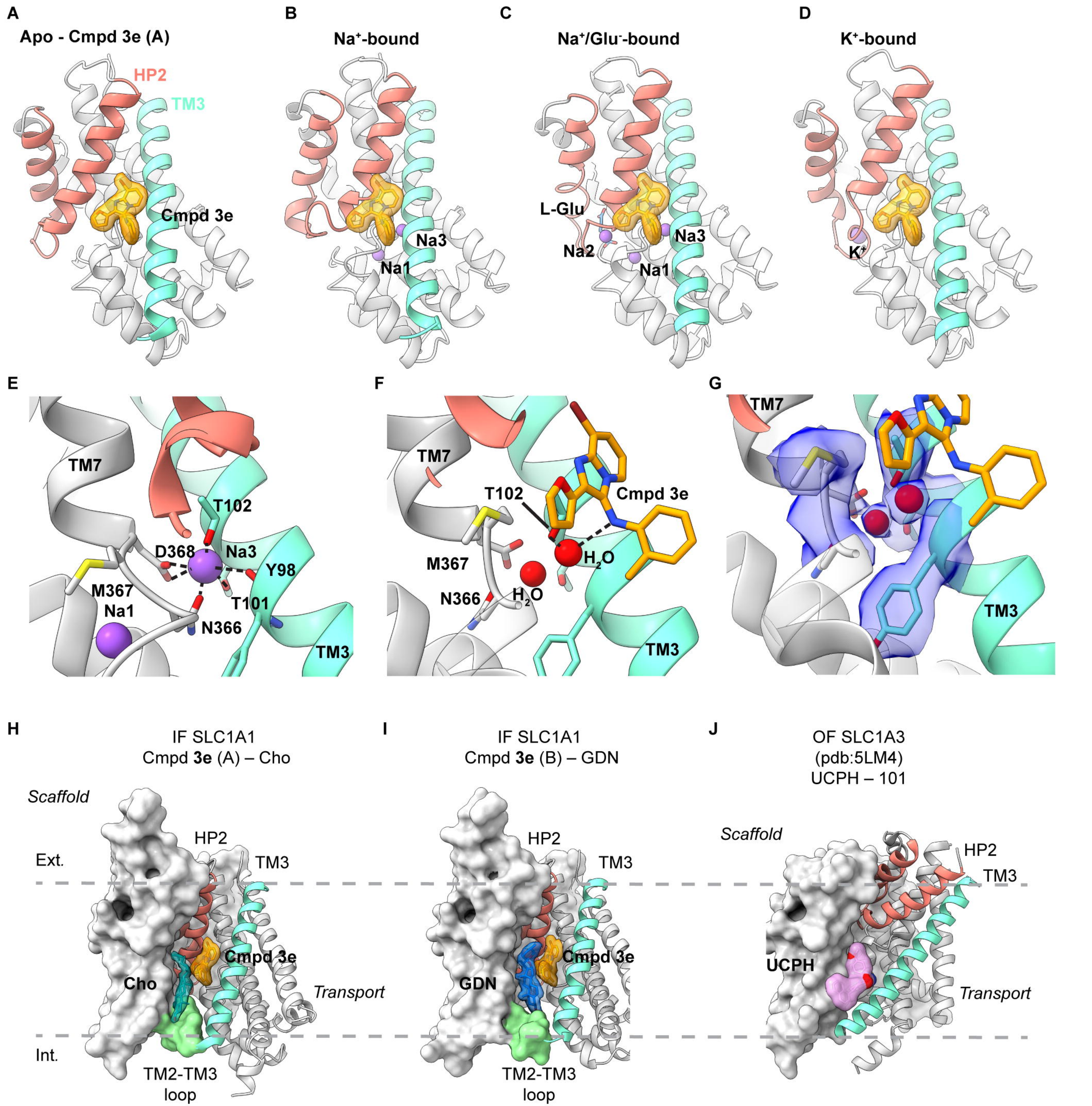
A
Apo - Cmpd 3e (A)
HP2
TM3
Cmpd 3e
B
Na+-bound
Na3
Na1
C
Na+/Glu--bound
L-Glu
Na2
Na3
Na1
D
K+-bound
K+
E
TM7
T102
D368
Na3
Y98
M367
Na1
T101
N366
TM3
F
TM7
T102
Cmpd 3e
M367
H2O
N366
H2O
TM3
G
TM7
TM3
H
IF SLC1A1
Cmpd 3e (A) – Cho
Scaffold
HP2
Ext.
TM3
Cmpd 3e
Cho
Transport
Int.
TM2-TM3
loop
I
IF SLC1A1
Cmpd 3e (B) – GDN
HP2
TM3
Cmpd 3e
GDN
TM2-TM3
loop
J
OF SLC1A3
(pdb:5LM4)
UCPH – 101
Scaffold
HP2
TM3
UCPH
Transport

FIGURE 3

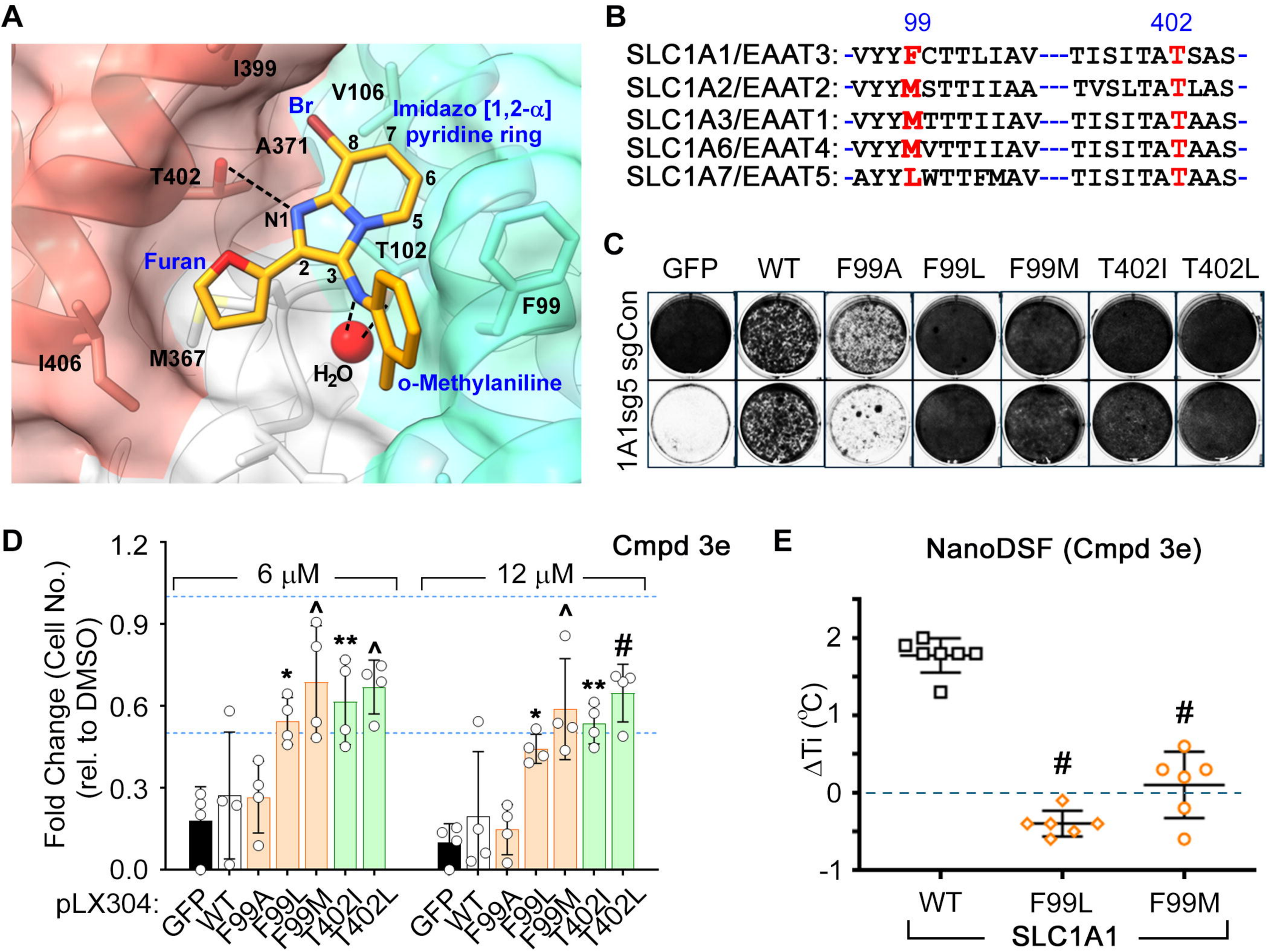
A
I399
V106
Br
Imidazo [1,2-α]
7 pyridine ring
A371
8
T402
6
N1
5
T102
Furan
2
3
F99
I406
M367
H2O
o-Methylaniline
B
99
402
SLC1A1/EAAT3: -VYYFCTTLIAV---TISITATSAS-
SLC1A2/EAAT2: -VYYMSTTIIAA---TVSLTATLAS-
SLC1A3/EAAT1: -VYYMTTTIIAV---TISITATAAS-
SLC1A6/EAAT4: -VYYMVTTIIAV---TISITATAAS-
SLC1A7/EAAT5: -AYYLWTTFMAV---TISITATAAS-
C
GFP
WT
F99A
F99L
F99M
T402I
T402L
1A1sg5 sgCon
D
Cmpd 3e
6 μM
12 μM
Fold Change (Cell No.) (rel. to DMSO)
1.2
0.9
0.6
0.3
0.0
pLX304:
GFP
WT
F99A
F99L
F99M
T402I
T402L
E
NanoDSF (Cmpd 3e)
ΔTi (°C)
2
1
0
-1
WT
F99L
F99M
SLC1A1

FIGURE 4

A

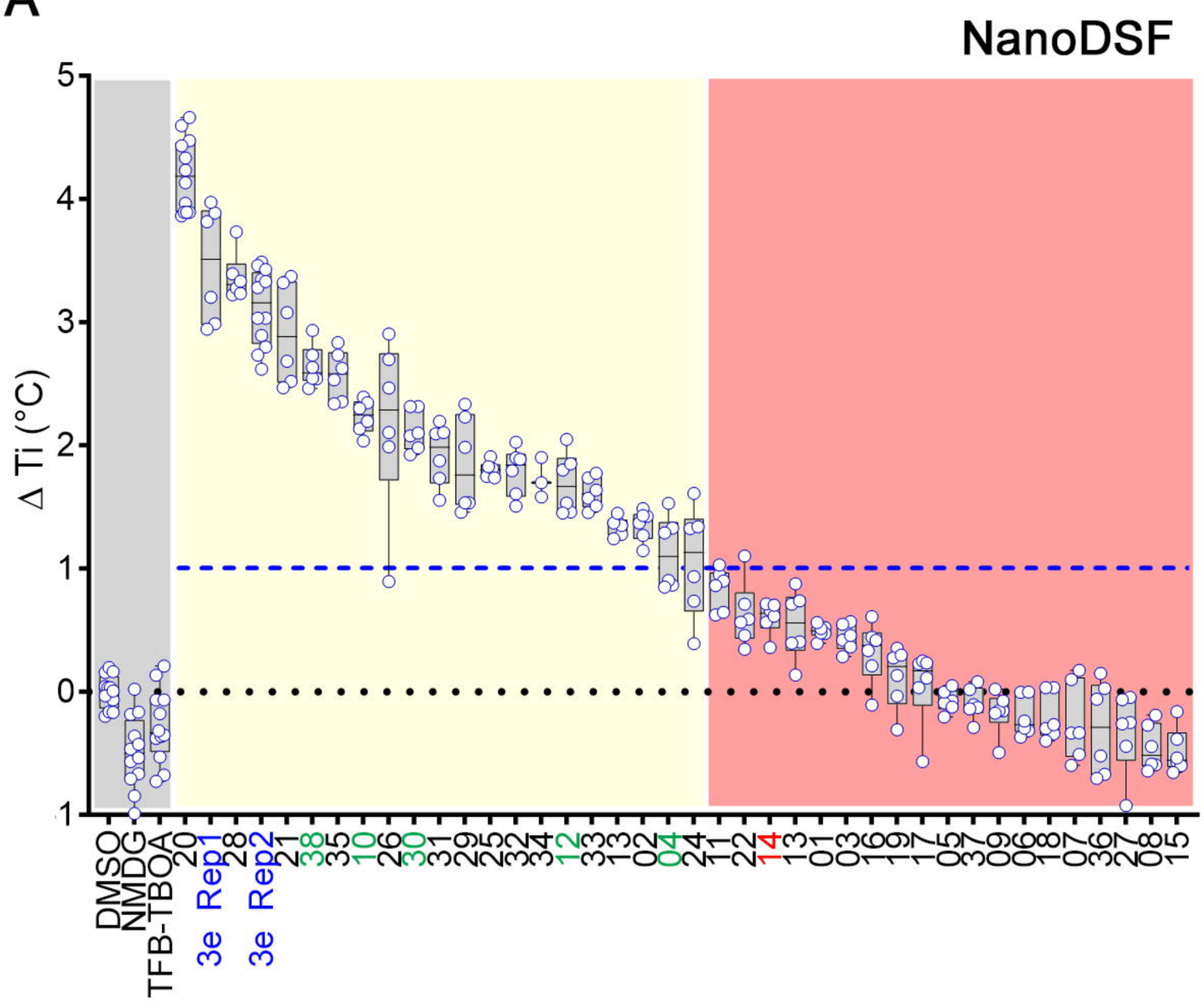

B

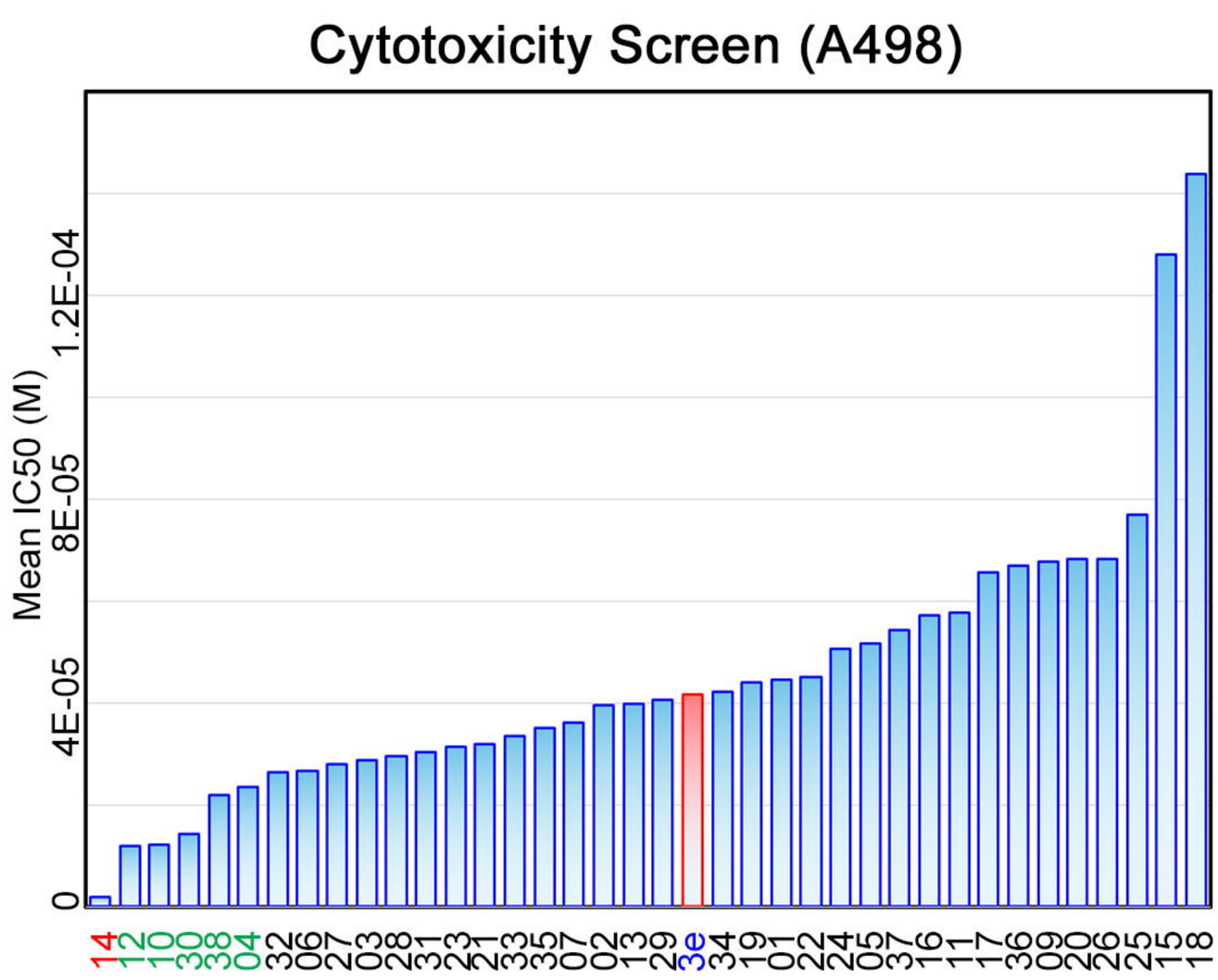

C

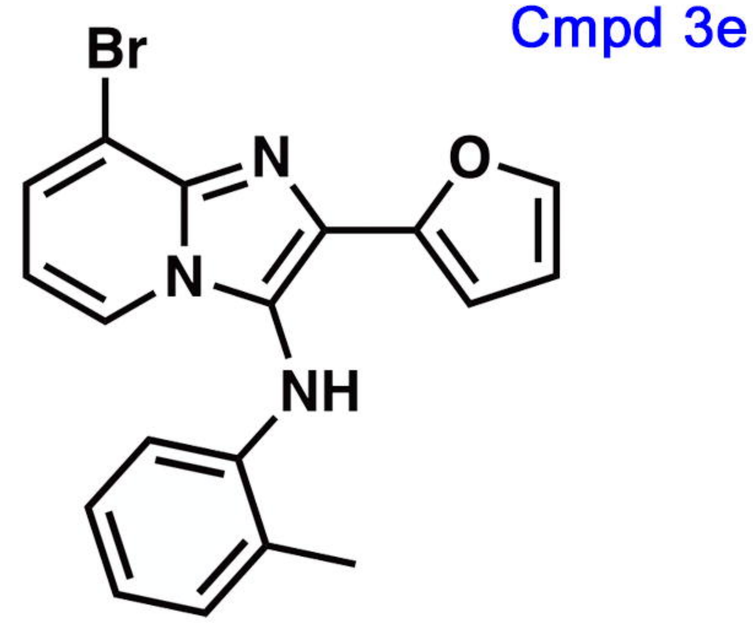

D

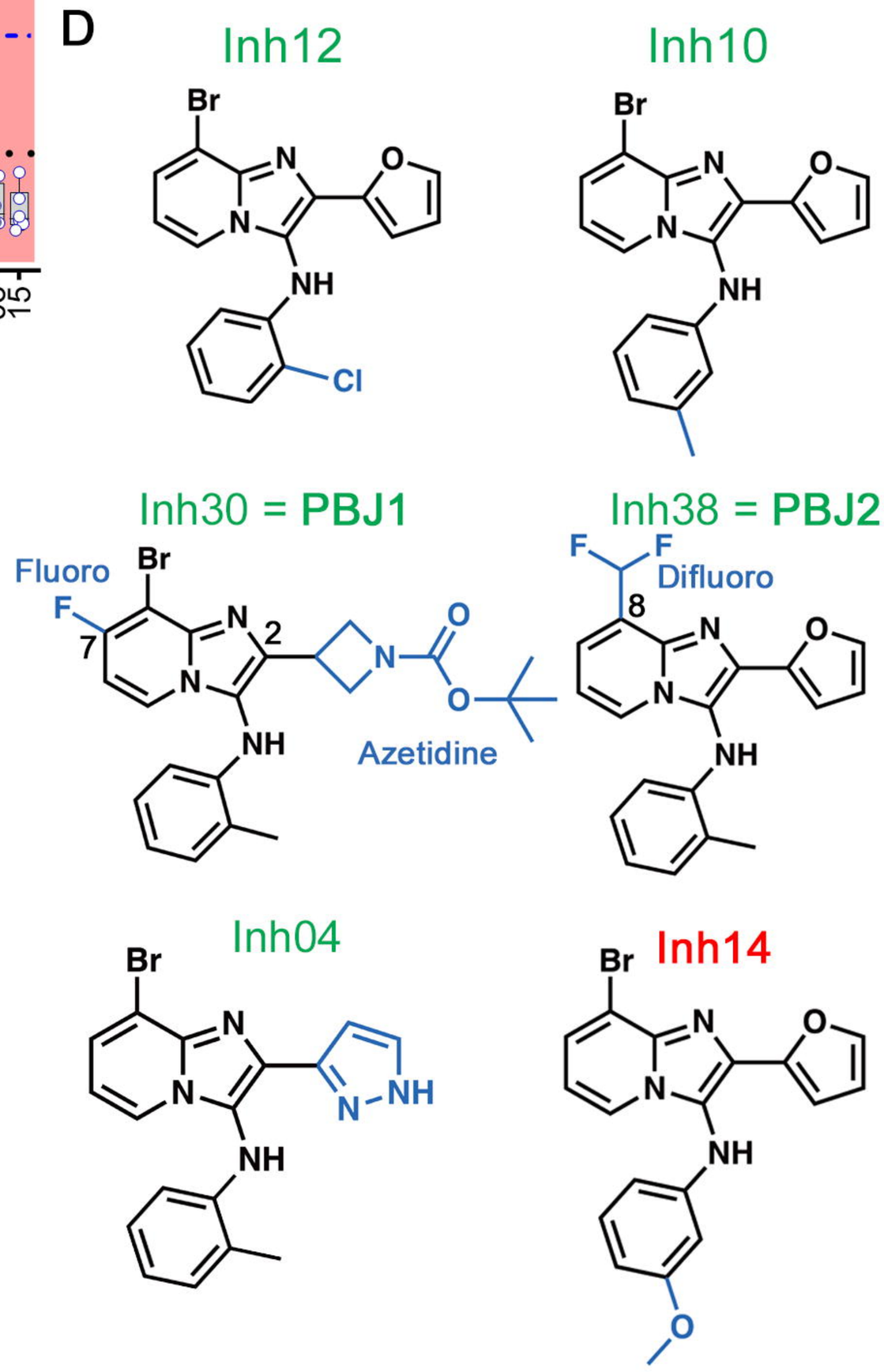

FIGURE 5

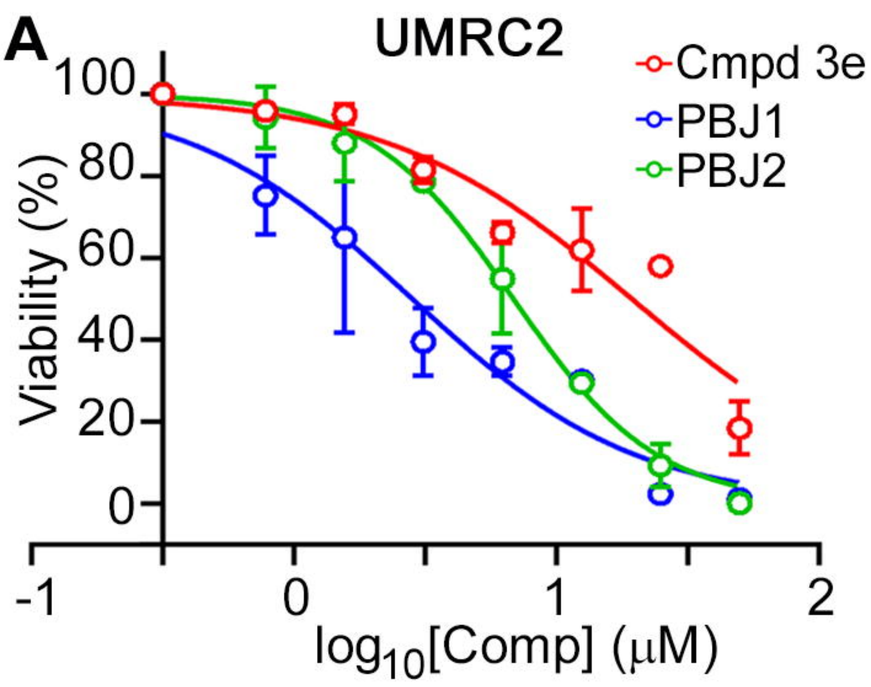

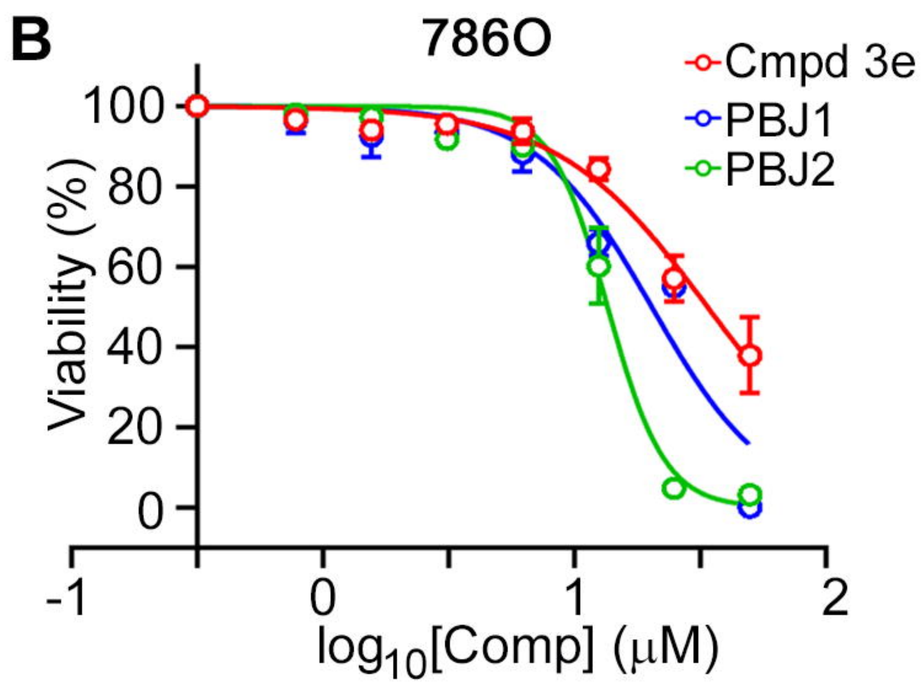

C

IC_{50} Values

		UMRC2	786O
Cmpd 3e	Best Fit	19.1	39.4
	95% CI	14.6-25.2	32.1-48.9
PBJ1	Best Fit	2.8	20.7
	95% CI	2.1-3.9	8.4-21.0
PBJ2	Best Fit	6.8	13.2
	95% CI	5.1-8.9	14.3-30.3

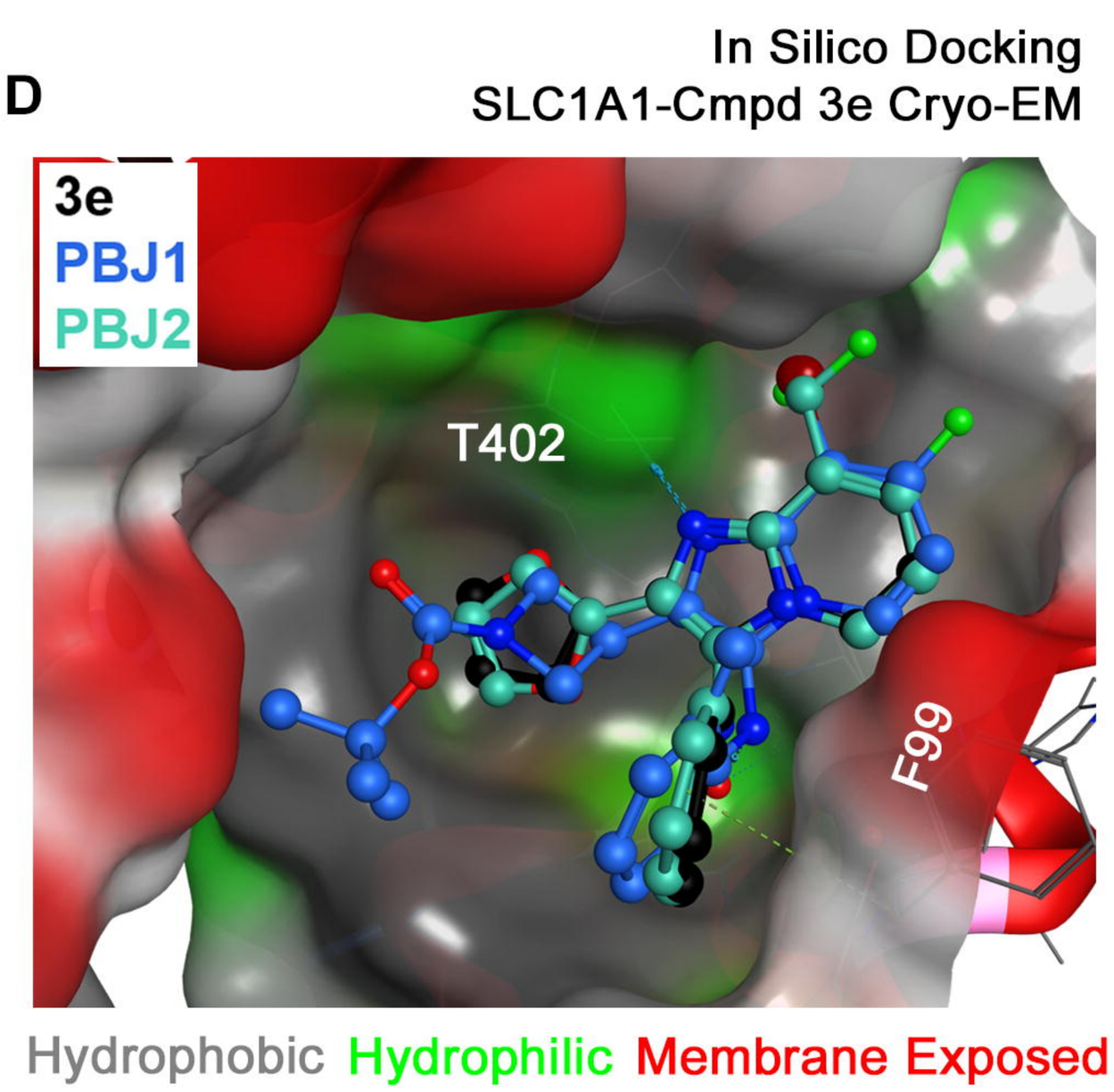

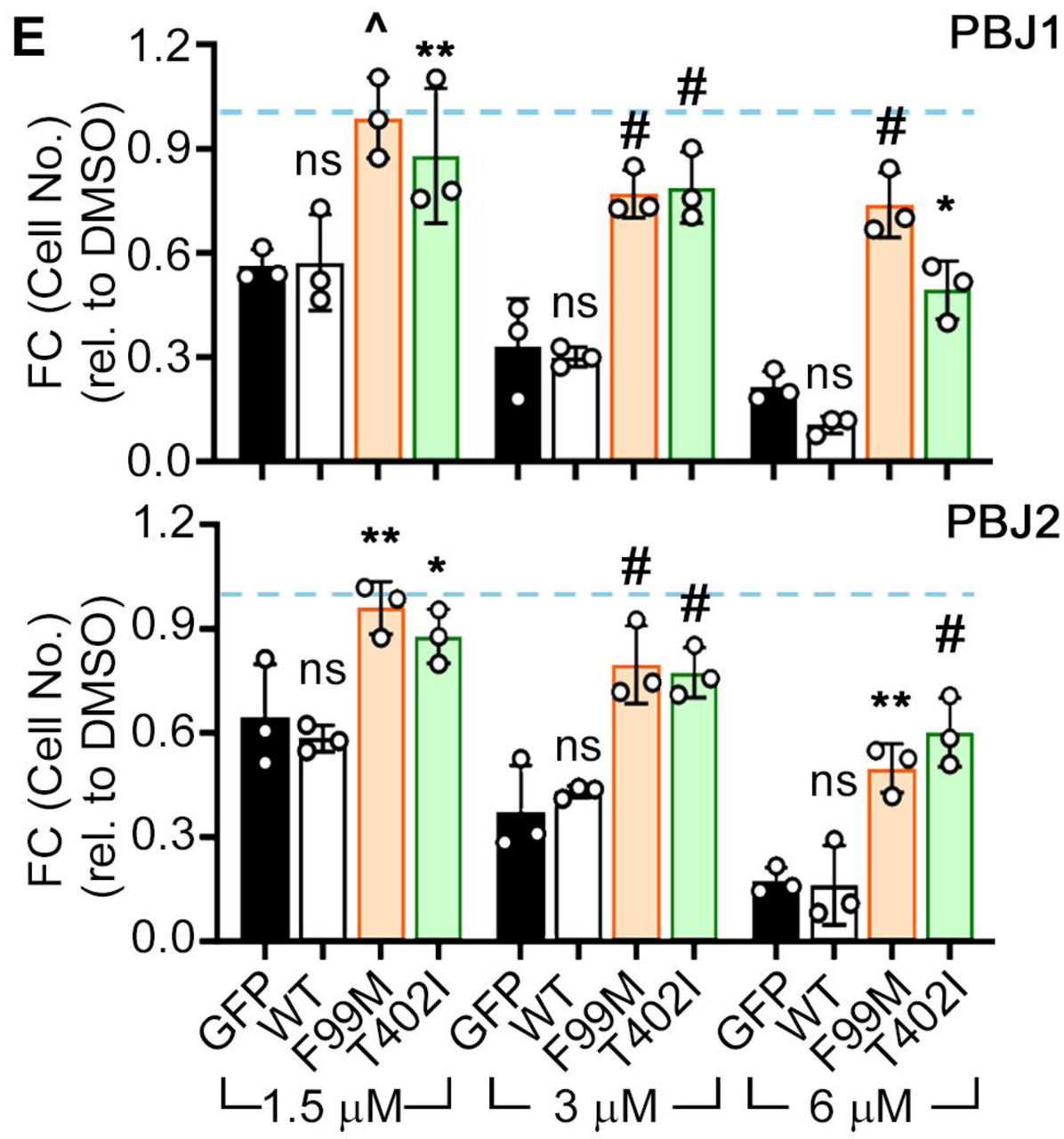

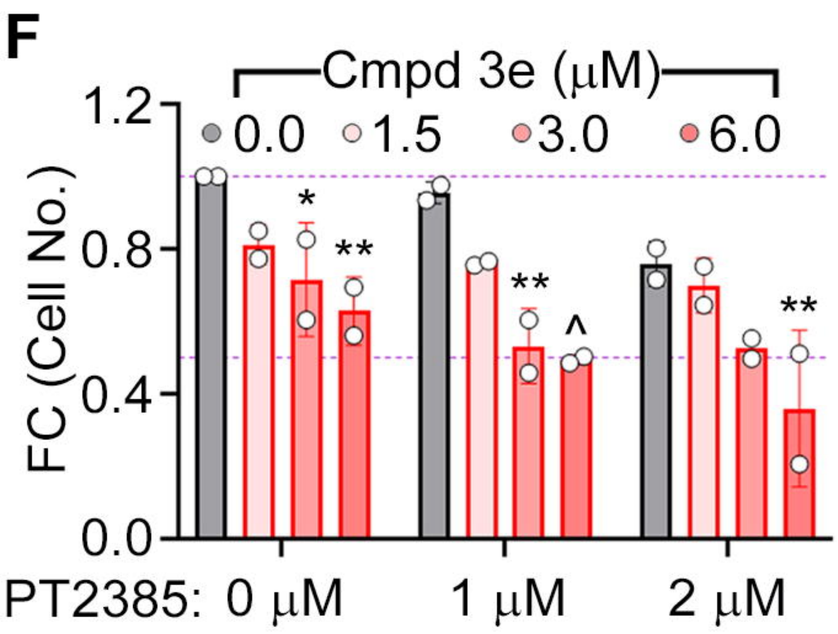

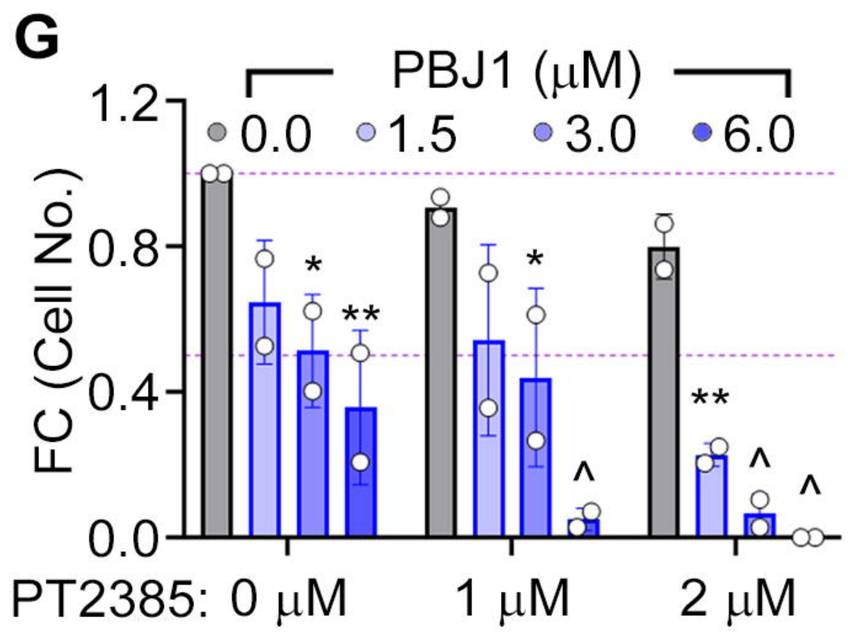

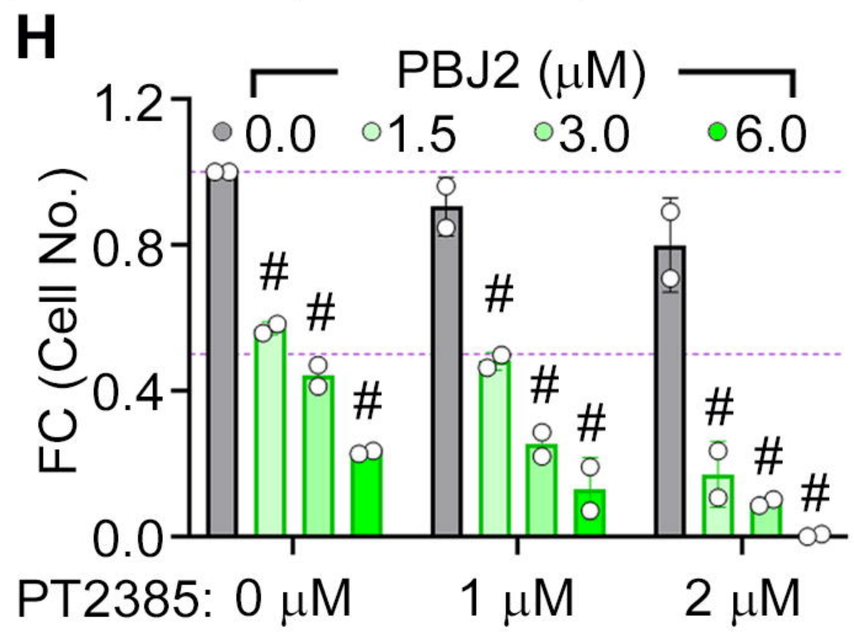

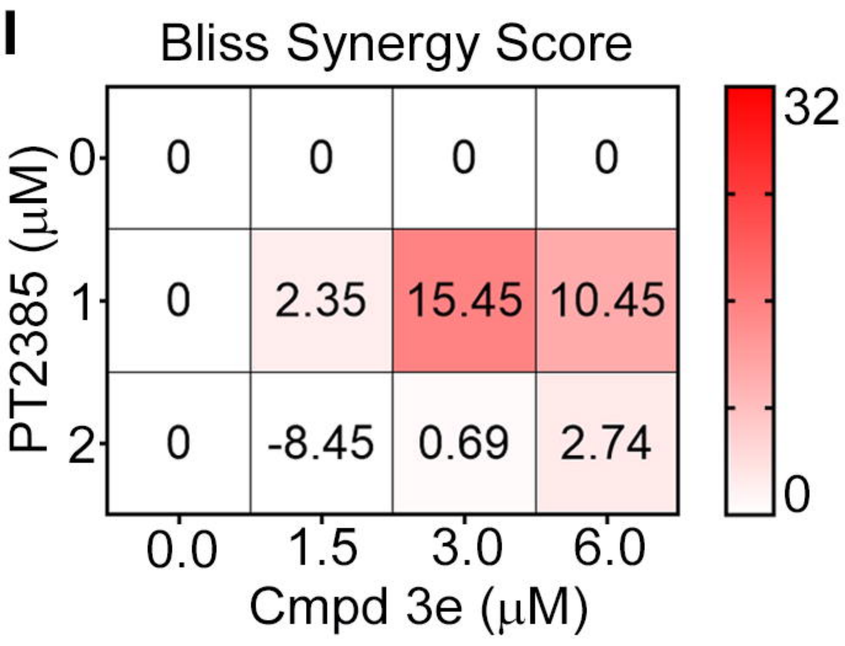

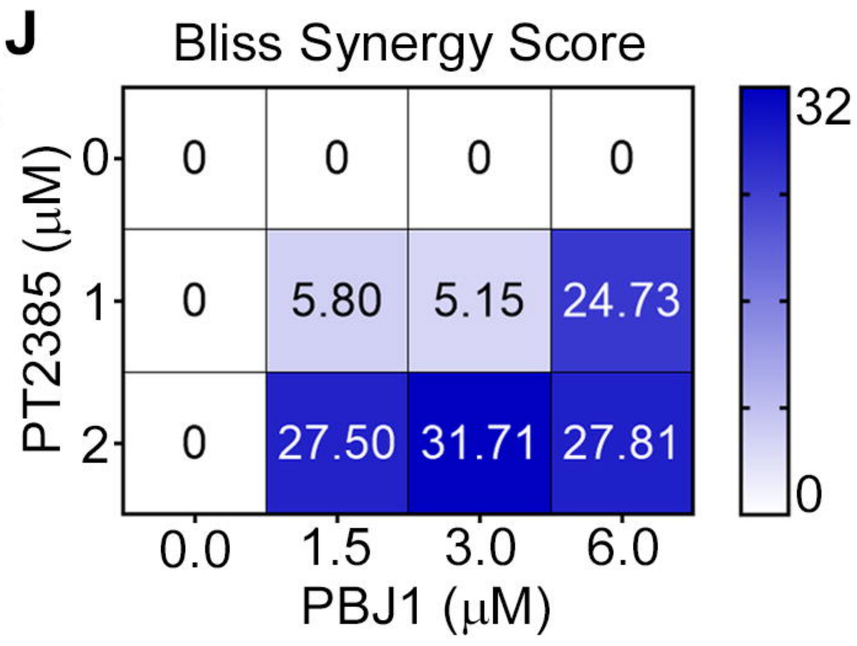

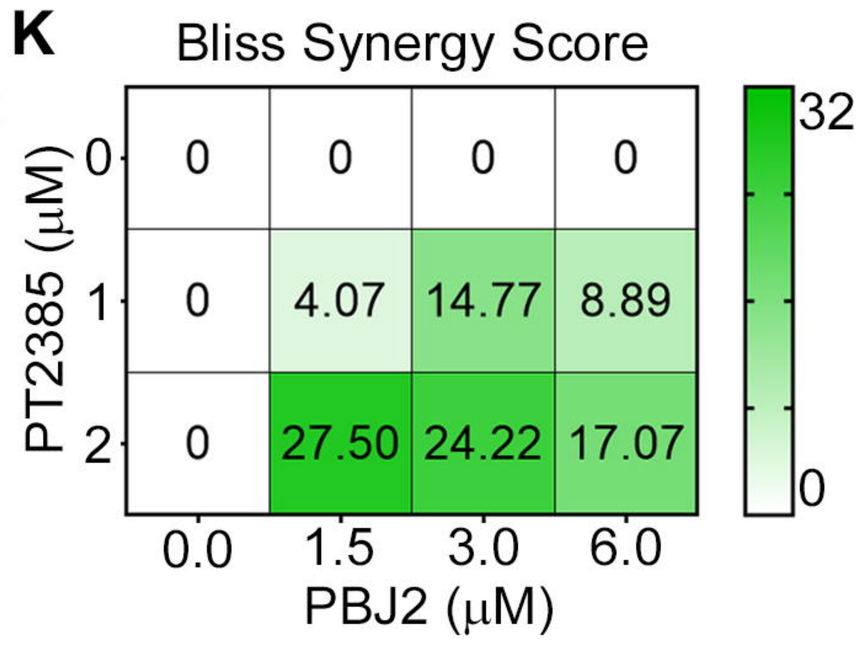

FIGURE 6

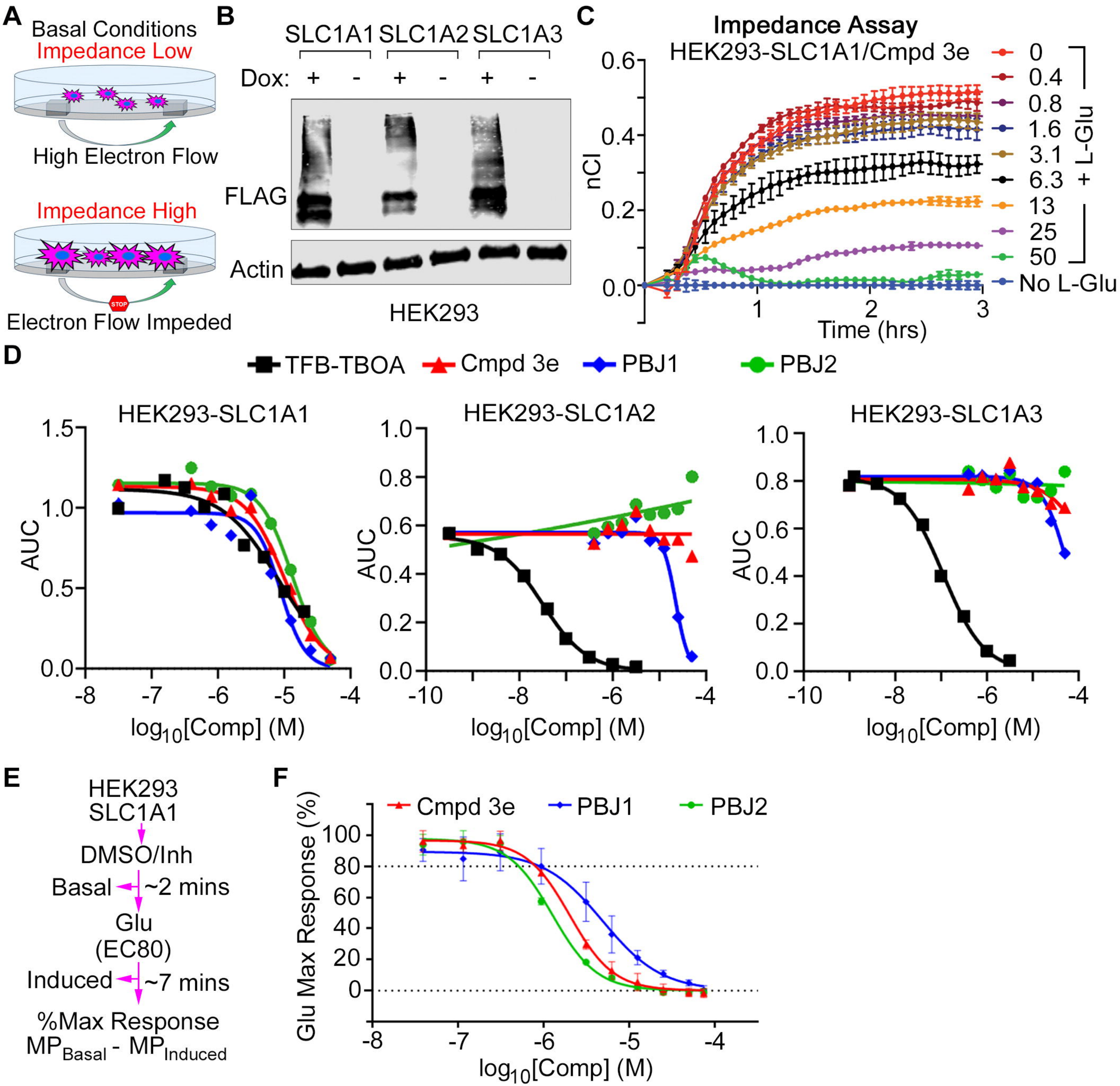
A
Basal Conditions
Impedance Low
High Electron Flow
Impedance High
STOP
Electron Flow Impeded
B
SLC1A1 SLC1A2 SLC1A3
Dox: + - + - + -
FLAG
Actin
HEK293
C
Impedance Assay
HEK293-SLC1A1/Cmpd 3e
nCI
Time (hrs)
0
0.4
0.8
1.6
3.1
6.3
13
25
50
No L-Glu
+ L-Glu
D
TFB-TBOA
Cmpd 3e
PBJ1
PBJ2
HEK293-SLC1A1
HEK293-SLC1A2
HEK293-SLC1A3
AUC
log10[Comp] (M)
E
HEK293
SLC1A1
DMSO/Inh
Basal
~2 mins
Glu
(EC80)
Induced
~7 mins
%Max Response
MPBasal - MPInduced
F
Cmpd 3e
PBJ1
PBJ2
Glu Max Response (%)
log10[Comp] (M)

FIGURE 7

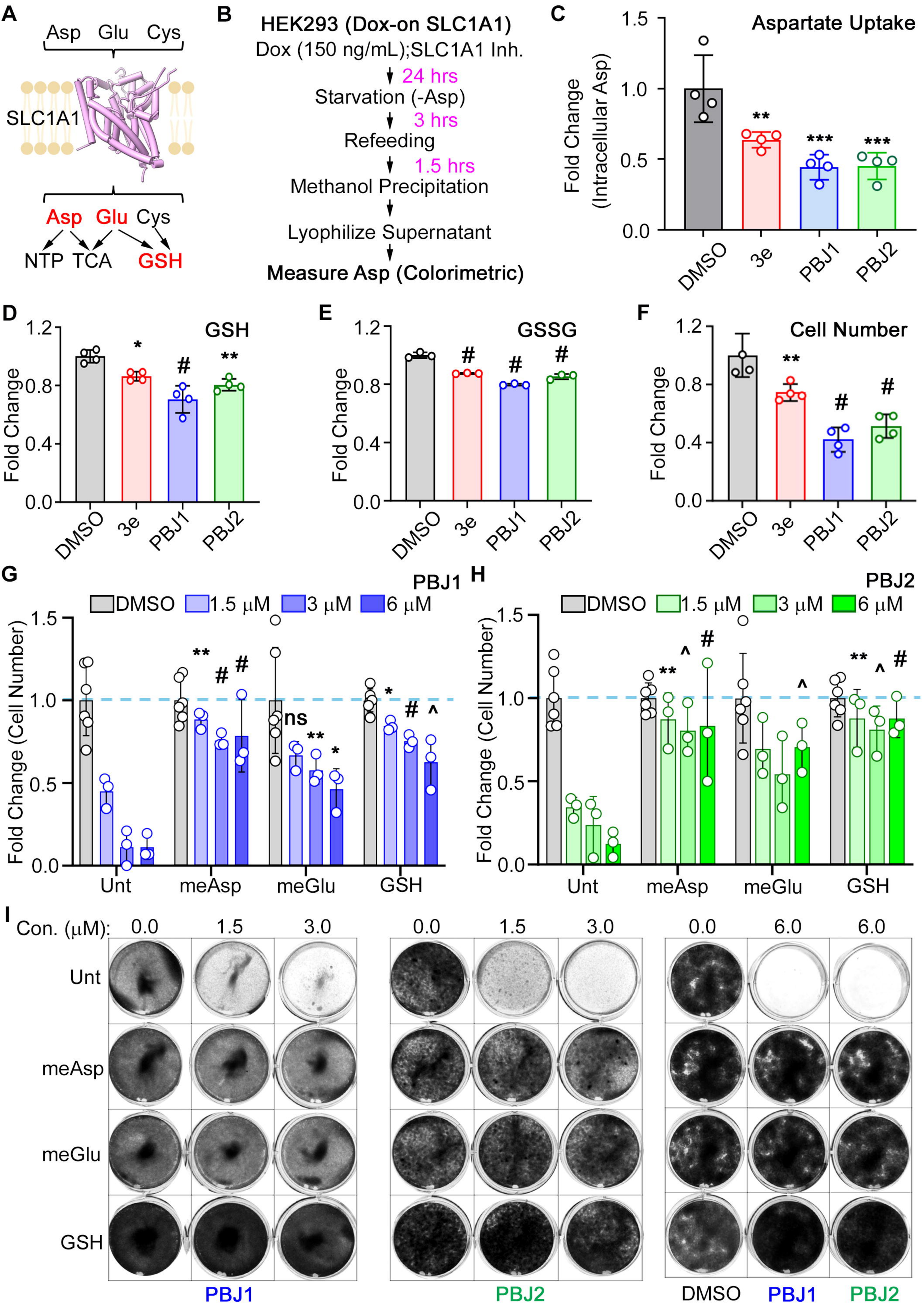
A
Asp Glu Cys
SLC1A1
Asp Glu Cys
NTP TCA GSH
B
HEK293 (Dox-on SLC1A1)
Dox (150 ng/mL);SLC1A1 Inh.
24 hrs
Starvation (-Asp)
3 hrs
Refeeding
1.5 hrs
Methanol Precipitation
Lyophilize Supernatant
Measure Asp (Colorimetric)
C
Aspartate Uptake
Fold Change (Intracellular Asp)
DMSO 3e PBJ1 PBJ2
D
GSH
Fold Change
E
GSSG
F
Cell Number
G
DMSO 1.5 μM 3 μM 6 μM
Fold Change (Cell Number)
Unt meAsp meGlu GSH
ns
H
PBJ1
PBJ2
I
Con. (μM): 0.0 1.5 3.0 0.0 1.5 3.0 0.0 6.0 6.0
Unt
meAsp
meGlu
GSH
PBJ1
PBJ2
DMSO PBJ1 PBJ2